

Expanded Sample of Small Magellanic Cloud Ultraviolet Dust Extinction Curves: Correlations between the 2175 Å bump, Q_{PAH} , UV extinction shape, and $N(HI)/A(V)$

KARL D. GORDON,^{1,2} E. L. FITZPATRICK,³ DERCK MASSA,⁴ RALPH BOHLIN,¹ JÉRÉMY CHASTENET,² CLAIRE E. MURRAY,^{1,5}
GEOFFREY C. CLAYTON,⁶ DANIEL J. LENNON,^{7,8} KARL A. MISSELT,⁹ AND KARIN SANDSTROM¹⁰

¹Space Telescope Science Institute, 3700 San Martin Drive, Baltimore, MD, 21218, USA

²Sterrenkundig Observatorium, Universiteit Gent, Gent, Belgium

³Department of Astronomy & Astrophysics, Villanova University, 800 Lancaster Avenue, Villanova, PA 19085, USA

⁴Space Science Institute, 4750 Walnut Street, Suite 205, Boulder, CO 80301, USA

⁵Department of Physics & Astronomy, Johns Hopkins University, 3400 N. Charles Street, Baltimore, MD 21218

⁶Department of Physics & Astronomy, Louisiana State University, Baton Rouge, LA 70803, USA

⁷Instituto de Astrofísica de Canarias, 38 200, La Laguna, Tenerife, Spain

⁸Dpto. Astrofísica, Universidad de La Laguna, 38 205, La Laguna, Tenerife, Spain

⁹Steward Observatory, University of Arizona, Tucson, AZ 85721, USA

¹⁰Department of Astronomy & Astrophysics, University of California, San Diego, 9500 Gilman Drive, San Diego, CA 92093, USA

ABSTRACT

The Small Magellanic Cloud (SMC) shows a large variation in ultraviolet (UV) dust extinction curves, ranging from Milky Way-like (MW) to significantly steeper curves with no detectable 2175 Å bump. This result is based on a sample of only nine sightlines. From HST/STIS and IUE spectra of OB stars, we have measured UV extinction curves along 32 SMC sightlines where eight of these curves were published previously. We find 16 sightlines with steep extinction with no detectable 2175 Å bump, four sightlines with MW-like extinction with a detectable 2175 Å bump, two sightlines with fairly flat UV extinction and weak/absent 2175 Å bumps, and 10 sightlines with unreliable curves due to low SMC dust columns. Our expanded sample shows that the sightlines with and without the 2175 Å bump are located throughout the SMC and not limited to specific regions. The average extinction curve of the 16 bumpless sightlines is very similar to the previous average based on four sightlines. We find no correlation between dust column and the strength of the 2175 Å bump. We test the hypothesis that the 2175 Å bump is due to the same dust grains that are responsible for the mid-infrared carbonaceous (PAH) emission features and find they are correlated, confirming recent work in the MW. Overall, the slope of the UV extinction increases as the amplitudes of the 2175 Å bump and far-UV curvature decrease. Finally, the UV slope is correlated with $N(HI)/A(V)$ and the 2175 Å bump and nonlinear far-UV rise amplitudes are anti-correlated with $N(HI)/A(V)$.

Keywords: interstellar dust, interstellar dust extinction, ultraviolet extinction, Small Magellanic Cloud

1. INTRODUCTION

Dust grains modulate the flow of radiation through a galaxy, affecting the general ISM structure, the environments of star formation, and the overall energy balance. In addition, dust complicates our ability to understand the properties of the stellar populations and interstellar gas. Characterizing the wavelength-dependence of dust extinction can enable us to correct for its effects and provide observational constraints on dust grain size distributions.

Investigating the dust extinction in external galaxies, in conjunction with Milky Way (MW) studies, is important because it increases the range over which quantifiable environmental factors (e.g., metallicity, gas-to-dust ratio, IR intensities, $H\alpha$ intensity, etc.) can be correlated with extinction properties and the properties of the grain populations themselves (e.g., grain size, shape, and composition). This, in

turn, increases our understanding of the sensitivity of dust grains to environmental factors and also leads to a measure of predictability - i.e., certain environmental factors may yield certain extinction properties - which is useful for correcting for dust's effects on observations of stars and gas.

Ultraviolet extinction curves have been determined in the Local Group of galaxies for the MW, the Large Magellanic Cloud (LMC), the Small Magellanic Cloud (SMC), and M31. The extinction curves in these galaxies paint a complex picture of the environmental dependence of dust properties. In the MW, the near-infrared to UV extinction curves can be described fairly well by a relationship that depends on only one parameter, $R(V) = A(V)/E(B - V)$, which is a measure of the overall dust grain size (Cardelli et al. 1989; Valencic et al. 2004; Fitzpatrick et al. 2019; Gordon et al. 2023). There are significant deviations from the $R(V)$ relationship

in different Galactic environments (Mathis & Cardelli 1992; Valencic et al. 2004) including one sightline that (after foreground extinction is removed) is similar to the traditional SMC curve (Valencic et al. 2003). In the LMC, the UV extinction curves show a distinctly different behavior between the LMC 2 (roughly 30 Dor region) and the rest of the LMC (Fitzpatrick 1985; Fitzpatrick & Massa 1986; Misselt et al. 1999). The 2175 Å bump is much weaker in the LMC 2 region, whereas the rest of the LMC shows curves similar to the average Galactic extinction curve. The SMC has two kinds of curves: the traditional SMC curve without a 2175 Å bump and those with a recognizable 2175 Å bump (Gordon et al. 2003; Maíz Apellániz & Rubio 2012). In M31, recent work has found two extinction curves consistent with the MW average and two that are similar to the LMC 2 average (Clayton et al. 2015). The extinction curve behavior in these four galaxies implies that the physical properties of dust grains are likely to be dependent on a multitude of environmental parameters. These include the gas-to-dust ratio, metallicity, and star formation activity, all of which may affect the overall composition and size distribution of dust grains (Gordon et al. 1997, 2003).

In recent years, observations of UV extinction in distant galaxies have advanced from, first, noting the absence of the 2175 Å bump in many starburst and Lyman Break galaxies (Calzetti et al. 1994; Gordon et al. 1997; Vihj et al. 2003) to more recent detections of the bump in the spectra of high redshift galaxies and an anti-correlation between its strength and galaxy luminosity (e.g., Noll et al. 2007, 2009; Buat et al. 2012; Kriek & Conroy 2013; Witstok et al. 2023; Markov et al. 2023) and the discovery of strong bumps in the dust extinction of high-redshift gamma ray bursts (e.g., Elíasdóttir et al. 2009; Schady et al. 2012; Zafar et al. 2012). The emerging picture of dust extinction properties in distant galaxies is not unlike that seen in the Local Group, i.e., extreme regional variations suggesting significant internal variations in the basic properties of the interstellar grain populations. In addition, strong galaxy-to-galaxy trends suggest that global properties, such as metallicity and recent star formation activity, may also play a significant role in shaping the dust and resultant extinction properties.

The SMC is a critical galaxy in which to study dust properties. It has been known for many years to have UV extinction curves that differ the most from typical MW extinction (Lequeux et al. 1982; Prevot et al. 1984) suggesting systematically different grain properties. It is also an ideal laboratory for investigating the nature of the 2175 Å bump carrier, as the SMC shows the largest range of 2175 Å bump strengths of any Local Group galaxy, indicating large internal variations in grain properties. In addition, it has a significantly lower metallicity than the MW (Russell & Dopita 1992; Domínguez-Guzmán et al. 2022) and such a chemically primitive environment may be more similar to that in more distant galaxies (e.g., gamma-ray burst host galaxies). Thus, the SMC could provide an important link between the dust grain and extinction properties in the nearby uni-

verse with those of the observationally less accessible distant galaxies.

Given its importance, it is somewhat surprising that the published sample of UV extinction curves for the SMC is small, with a total of only 9 sightlines. This sample is composed of four sightlines created from *International Ultraviolet Explorer* spectroscopic observations (Gordon & Clayton 1998), one sightline created from *Hubble Space Telescope* (HST) *Space Telescope Imaging Spectrograph* (STIS) slit spectroscopy observations (Gordon et al. 2003), and four sightlines created by fitting HST/STIS slitless prism spectroscopy observations (Maíz Apellániz & Rubio 2012). These show large differences in UV extinction strengths, especially in the 2175 Å bump and far-UV rise features. Roughly, these nine curves can be categorized into three that are similar to those seen in the MW with recognizable 2175 Å bumps (AzV 456, MR12 09, 10) and six that are roughly linear with λ^{-1} and lack a 2175 Å bump (AzV 18, 23, 214, 398, MR12 08, 11). Based on the 5 sightlines known at the time, Gordon et al. (2003) postulated that the differences could be due to processing from nearby star formation since all the sightlines without 2175 Å bumps were in the SMC’s star-forming Bar and the remaining sightline with a 2175 Å bump was in the more quiescent SMC Wing. This interpretation was clearly too simple as the 4 sightlines studied by Maíz Apellániz & Rubio (2012) were all in a small region in the SMC’s star-forming Bar and split evenly between those with and without a 2175 Å bump. Clearly, the small sample of measured UV extinction curves is the major limitation in studying the UV extinction properties in the SMC.

In this paper, we present UV through near-IR extinction curves for the sightlines towards 32 stars, greatly enhancing the previously available sample. In the past, one of the main deterrents to measuring SMC extinction curves was the lack of large numbers of high quality stellar spectral types, making it difficult to identify reddened stars. In recent years, however, the number of stars with good spectral types has increased dramatically, largely due to the 2dF survey of more than 4,000 SMC stars (Evans et al. 2004), plus a number of VLT-FLAMES surveys (Evans et al. 2006; Martayan et al. 2007). This better characterization of the SMC’s hot star population – from which multiband extinction curves are derived – provided a main motivation for this work.

In §2 we describe new *HST/STIS* UV spectrophotometric observations for 19 SMC stars, along with the data processing techniques. This section also gives the details of the archival *IUE* and *HST/STIS* spectra used here and ancillary data for the entire sample. In §3, we present the calculation of the extinction curves, the correction for MW foreground extinction, the best-fitting stellar and extinction parameters, and a comparison to previous work. The UV extinction behavior distribution across the SMC, sample average curves, and correlations with mid-IR carbonaceous (aka PAH) features are presented in §4. The behavior of the SMC UV extinction in context with results for the LMC and MW are analyzed in §5 focusing on the general sightline characteristics, the corre-

lations between UV extinction parameters, and correlations with gas-to-dust. Finally, the conclusions of this work are given in §6.

2. DATA

The sample of extinction curve sightlines is composed of all OB stars with spectroscopic observations covering the UV region from 1150 to 3100 Å with IUE or HST/STIS slit spectral observations. The STIS sample is composed of all the targets in our three HST programs on this subject (PIDs: 8198, 12258, and 14225; PI: Gordon). The targets in the first program were used to create extinction curves using the standard pair method and published by [Gordon et al. \(2003\)](#). The targets in the second and third programs are presented here for the first time. The IUE sample is composed principally of the reddened and comparison stars from [Gordon & Clayton \(1998\)](#) supplemented with two additional stars (SK 191 and BBB SMC 280) found by a careful followup search of the IUE archive for potential reddened targets. The names, coordinates, spectral types, and spectral type references for the sample are given in Table 1. The sources were taken from various catalogs specifically AzV ([Azzopardi et al. 1975](#)), 2dFS ([Evans et al. 2004](#)), MR12 ([Maíz Apellániz & Rubio 2012](#)), NGC330/NGC346 ([Evans et al. 2006](#)), SMC5 ([Martayan et al. 2007](#)), BBB ([Basinski et al. 1967](#)), and SK ([Sanduleak 1969](#)).

This sample represents the full set of SMC extinction curves currently measured using UV slit spectroscopy observations. The six sightlines in the STIS1 (PID 8198) program are described by [Gordon et al. \(2003\)](#). The sightlines in the STIS2 (PID 12258) program started with an initial sample of reddened OB main sequence and giant stars from the 2dF and VLT-FLAMES surveys ([Evans et al. 2004, 2006](#); [Martayan et al. 2007](#)). This initial sample was culled of stars with photometric mid-infrared excess (Be star, winds, etc.) using the SAGE-SMC survey ([Gordon et al. 2011](#)). A final sample of 15 reddened stars was chosen based on the desire to have high extinctions, span the spectral type range, spatially span the galaxy, and obtain HST/STIS observations in a reasonable amount of observing time. The planned four sightlines in the STIS3 (PID 14225) program were those in ([Maíz Apellániz & Rubio 2012](#)) with significant extinction. Unfortunately, the planned observations of one of these four (MR12 08) ended up observing the nearby multiple source MR12 06/07 that is only lightly extinguished, which was the brightest source in the STIS target acquisition 5x5'' field-of-view. Thus, only three of the four planned MR12 sightlines were observed.

Of the 35 stars in the sample, it was not possible to measure extinction curves for three of them (AzV 23, AzV 404, and MR12 06/07), due to their very low $E(B - V)$ values. Thus, while there are 35 stars in the sample, only 32 extinction curves are presented. The eight extinction curves previously published are designated in Table 1 with table notes giving the references. The UV spectra for all the program stars are plotted in Fig. 1. The details of the observational

Table 1. Sample Details

Name	RA (J2000) ^a	DEC (J2000) ^a	SpType	Ref
STIS Sample				
2dFS 413	00 42 15.81	-73 24 32.9	B1-5(IV)	1
2dFS 626	00 46 55.80	-73 06 14.6	B0-5(V)	1
2dFS 662	00 47 45.58	-73 13 37.2	B1-2(III)	1
2dFS 699	00 47 58.49	-72 31 41.8	B0.5(II)e	1
2dFS 3014	01 14 26.28	-73 17 13.5	B0-5(V)	1
2dFS 3030	01 14 40.14	-73 16 14.5	O7-8V	1
2dFS 3171	01 16 09.19	-73 12 38.8	B0(V)	1
AzV 4	00 45 03.30	-72 41 57.4	B2Ib	2
AzV 23 ^b	00 47 38.91	-73 22 53.9	B3Ia	3
AzV 86	00 51 05.83	-72 00 30.6	B1Ia	3
AzV 132	00 52 51.24	-73 06 53.6	B2	4
AzV 218	00 59 04.34	-72 19 40.8	B2Iab	2
AzV 404 ^d	01 06 29.26	-72 22 08.6	B2.5Iab	3
MR12 06/07 ^d	00 45 06.51	-73 18 24.6	B6-7	5
MR12 09 ^c	00 45 35.10	-73 18 36.0	B2.5-5	5
MR12 10 ^c	00 45 37.10	-73 18 40.0	B3-6	5
MR12 11 ^c	00 45 34.49	-73 18 41.8	B1.5-3	5
NGC330 ELS 110	00 56 20.67	-72 26 25.5	B2IV	6
NGC330 ELS 114	00 56 57.0	-72 25 31.7	B2III	6
NGC330 ELS 116	00 55 26.5	-72 27 33.7	B3III	6
NGC346 ELS 056 ^d	00 58 56.1	-72 09 33.8	B0V	6
SMC5-398	00 54 02.67	-72 25 40.8	B0.5III	7
SMC5-3739	00 57 13.85	-72 22 30.1	O9III	7
SMC5-79264	00 55 50.04	-72 19 23.7	B3III	7
SMC5-82923	00 53 26.17	-72 11 40.0	B0III	7
IUE Sample				
AzV 18 ^b	00 47 12.22	-73 06 33.1	B3Ia	2
AzV 70	00 50 18.12	-72 38 10.0	O9Ia	2
AzV 214 ^b	00 58 54.78	-72 13 17.2	B2Ia	2
AzV 289	01 01 58.78	-72 35 39.0	B0Ia	8
AzV 380	01 05 24.76	-73 03 53.0	B1Ia:	2
AzV 398 ^b	01 06 09.81	-71 56 00.7	O9Ia:	2
AzV 456 ^b	01 10 55.72	-72 42 56.1	O8II	2
AzV 462	01 11 25.92	-72 31 21.3	B2Ia	2
BBB SMC280	00 48 05.15	-73 12 03.6	B0-1(I)	9
SK 191	01 41 42.07	-73 50 38.2	B1.5Ia	3

^aCoordinates are from GAIA DR2 ([Gaia Collaboration 2018](#)) except for the NGC330/NGC346 sources ([Evans et al. 2006](#)).

^bExtinction curves previously published by [Gordon & Clayton \(1998\)](#) and [Gordon et al. \(2003\)](#).

^cExtinction curves based on STIS NUV prism data previously published by [Maíz Apellániz & Rubio \(2012\)](#).

^dExtinction curve could not be computed as the sightline $E(B - V)$ values were too low. Included for completeness as the STIS spectra were taken as part of the HST extinction curve programs.

References—(1) [Evans et al. \(2004\)](#), (2) [Smith Neubig & Bruhweiler \(1997\)](#), (3) [Lennon \(1997\)](#), (4) [Azzopardi et al. \(1975\)](#), (5) [Maíz Apellániz & Rubio \(2012\)](#), (6) [Evans et al. \(2006\)](#), (7) [Martayan et al. \(2007\)](#), (8) [Walborn \(1983\)](#), and (9) [Nandy et al. \(1982\)](#).

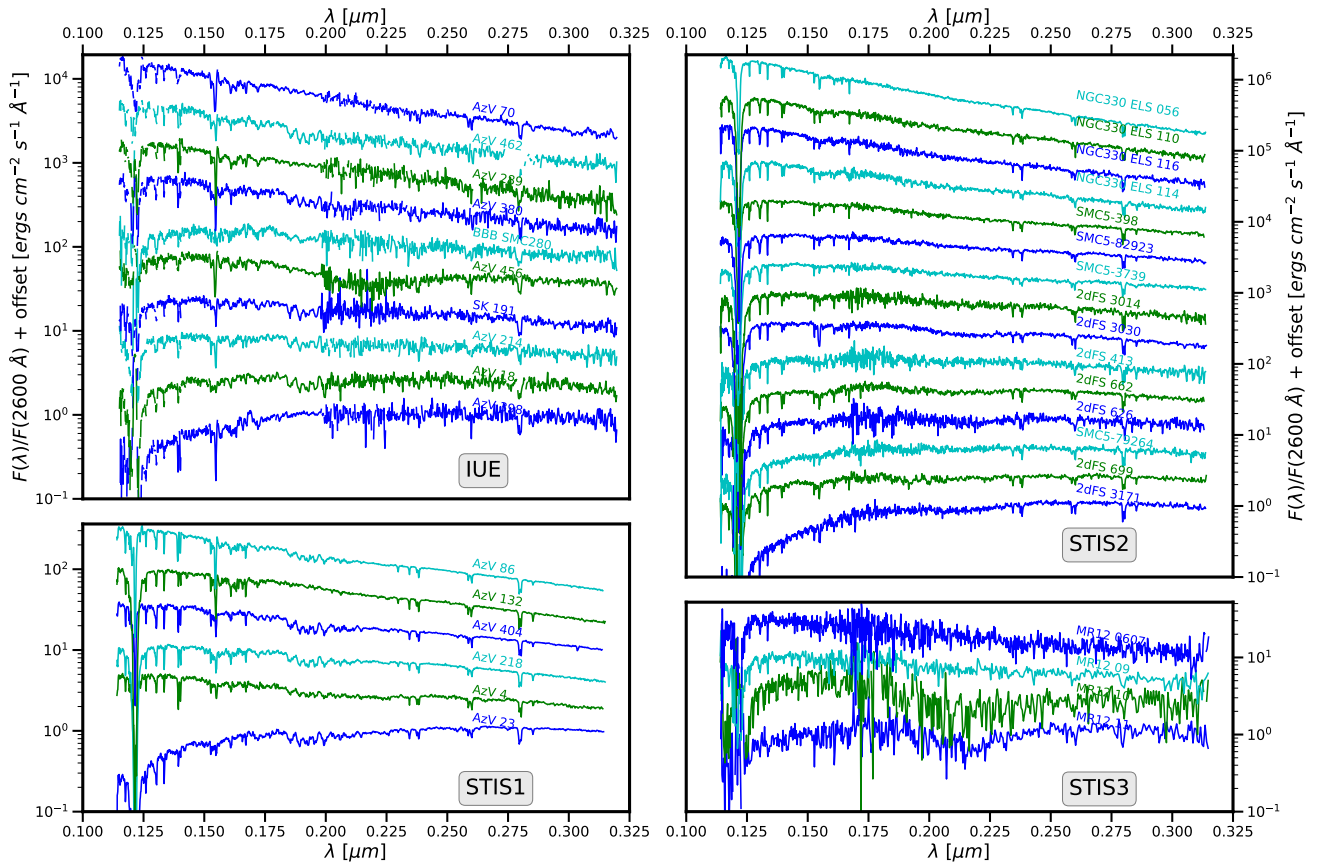


Figure 1. The UV spectra for all the stars in our sample. In each panel, the spectra are in order of UV spectral slope. This sorting shows all the spectra with little overlap and provides a rough ordering by amount of dust extinction. The IUE panel depicts all the IUE archival spectra; and the STIS1, STIS2, and STIS3 panels show the spectra from HST programs 8198, 12258, and 14225, respectively.

details and reduction of the IUE spectra are given by [Gordon & Clayton \(1998\)](#). The observational details and data reduction for the STIS spectra are given in the next section.

2.1. STIS Observations

STIS spectra of our program stars cover 1150–3180 Å at $R = 500 - 1000$ and utilize the low resolution G140L and G230L gratings with the 52X0.5, 52X2 or 2X2 slit (all slit dimensions are in arcsec). Our goal is to detect the 300-400 Å wide 2175 Å feature at 5σ for a 5% absorption depth. This goal translates to a signal-to-noise of 100 at $R = 10$ and defined the exposure times. For the brighter sources in our sample, longer exposure times were used to fill the HST orbit and potentially reveal weaker 2175 Å bumps.

The older observations of the AzV stars from HST proposal 8198 utilized the 52X0.5 slit, while the newer data from HST proposal 12258 used 2'' wide slits, which provide higher photometric accuracy ([Bohlin & Hartig 1998](#)). The avoidance of bright objects in the long 52X2 slit sometimes required the 2X2 entrance aperture; and the observations of 2DFS 699 and SMC5-3739 in both slits demonstrate the equivalence of the absolute fluxes. The geocoronal emis-

sion from Ly α at 1215.67 Å and from the much weaker OI line at 1302–1306 Å are imaged on top of the stellar signal; and the total background signal must be subtracted from the extracted gross signal to get the pure net stellar signal. The default background is the average of an upper and lower signal located 300 pixels above and below the spectral trace on the 1024x1024 pixel STIS images.

In the case of the 52X2 slit, the geocoronal sky is imaged and measured along with the residual background at all 1024 pixels. The background signal shortward of Ly α is fit with a cubic polynomial to the measurements from pixel 2–120, while a quartic polynomial is fit to the measurements longward of Ly α with the OI region excluded, i.e., the fit is for pixels 214–272 and 365–1023. The backgrounds in the lines at pixels 128–206 and at 280–356 are the averages in those two regions. Because the pixel ranges of the geocoronal lines varies by several pixels and because the emission profiles do not have perfectly sharp edges, there are a few pixels where the measured background must be used without any reduction of noise, i.e. at pixel ranges 121–127, 207–213, 273–279, and 357–364. For example, Figure 2 shows the measured background, the fitted background, and the net=gross-background in the Ly α region.

Table 2. HST STIS Observations

Name	Aperture	FUV		NUV	
		Rootname	Exposure (s)	Rootname	Exposure (s)
2DFS 413	52X2	objw07020	1729	objw07010	579
2DFS 626	2X2	objw06020	1919	objw06010	389
2DFS 662	2X2	objw09020	1931	objw09010	401
2DFS 699	52X2,2X2	objw11030,objw11040	850,850	objw11010,objw11020	150,150
2DFS 3014	52X2	objw08020	1729	objw08010	579
2DFS 3030	52X2	objw01020	1919	objw01010	389
2DFS 3171	52X2	objw04020	1725	objw04010	575
AzV 4	52X0.5	o5cg01030,o5cg01040	540,540	o5cg01010,o5cg01020	360,360
AzV 23	52X0.5	o5cg05010,o5cg05020	540,540	o5cg05030,o5cg05040	360,360
AzV 86	52X0.5	o5cg04010–50 ^a	120,100,100,120,120	o5cg04060–a0	120(5)
AzV 132	52X0.5	o5cg03010,o5cg03020	540,540	o5cg03030,o5cg03040	360,360
AzV 218	52X0.5	o5cg02010,o5cg02020	540,540	o5cg02030,o5cg02040	360,360
AzV 404	52X0.5	o5cg06010–50 ^a	144(5)	o5cg06060–a0	120(5)
MR12 06/07	52X2	ocxn01020	1547	ocxn01010	700
MR12 09	52X2	ocxn02020	1477	ocxn02010	780
MR12 10	52X2	ocxn03020	1535	ocxn03010	712
MR12 11	52X2	ocxn04020	1455	ocxn04010	800
NGC330 ELS 110	52X2	objw14020	1415	objw14010	885
NGC330 ELS 114	52X2	objw13020	1533	objw13010	767
NGC330 ELS 116	52X2	objw15020	1415	objw15010	885
NGC346 ELS 056	52X2	objw12020	1312	objw12010	1012
SMC5-398	2X2	objw05020	1801	objw05010	523
SMC5-3739	52X2,2X2	objw02030,objw02040	850,850	objw02010,objw02020	150,150
SMC5-79264	52X2	objw10020	1733	objw10010	397
SMC5-82923	2X2	objw03020	1801	objw03010	523

^a A sequence of 5 consecutive exposures for both G140L and G230L, where 120(5) indicates five exposures of 120 s.

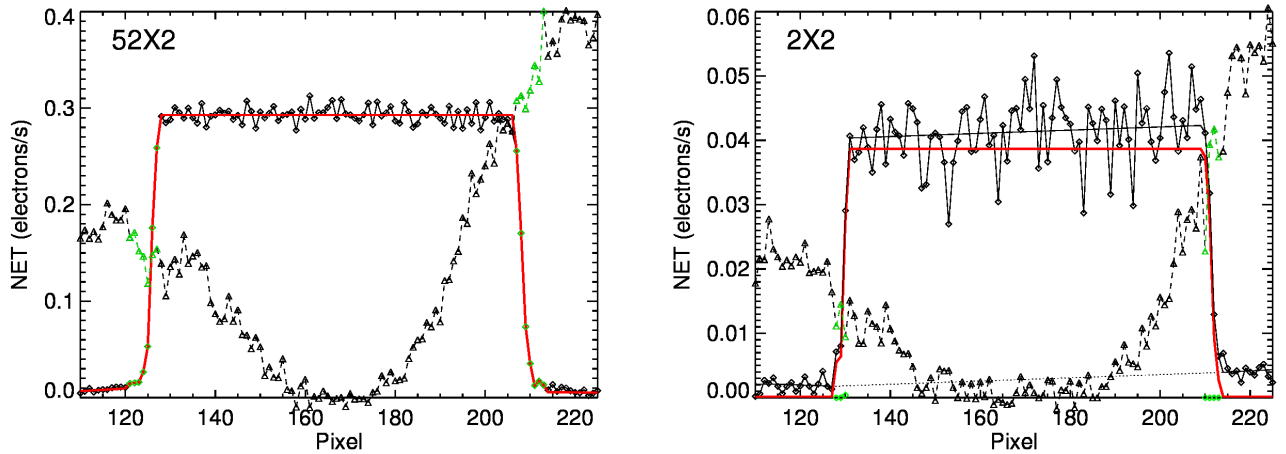


Figure 2. The sky background (diamonds) in the Ly α region and resulting final net signal (triangles) after subtracting the sky for an observation using the 52X2 slit (left, objw13020, NGC330 ELS 114) and one using the 2X2 slit (right, objw11040, 2DFS 0699). For the case of the long 52x2 slit, the sky background signal (red line) in the emission line regions is the measured average at 300 pixels above and below the spectral trace, except for the steep edges of the Ly α slit image (green points). To isolate the pure Ly α sky signal (red line) in the case of the 2X2 slit, the solid grey line fit to the diamonds is corrected for the stellar contribution by the dotted grey line that is fit to the pure stellar signal outside the emission region and used as an interpolation across the broad geo-coronal Ly α sky region.

In the case of the 52X0.5 slit, the geocoronal sky is flat within the noise at 159–175 and 311–326 pixel regions, while the background can be smoothly fit at 2–153, 182–272, and beyond 365.

In the case of the short 2X2 slit, the measured sky at 300 pixels from the spectral trace has no emission line signal and can be fit with one quartic polynomial. In order to estimate the emission line strengths for adding to this standard baseline, a near background is extracted at 32 pixels ($\sim 0.8''$) from the center with a width of 11 pixels, which keeps this background extraction region within the $2''$ slit. Following the procedure used for the 52X2 slit and due to the wings of the STIS PSF extending into the near background region, for the 2x2 slit this region requires a cubic at pixels 2–127 and a quartic at 214–272 and 365–1023. This near background as interpolated across the sky lines defines the subtraction at pixels 128–213 and at 273–364, which is added to the measured sky at 300 pixels to get the final total background that is subtracted from the gross signal. For example, the flat part of the Ly α in this difference is at pixels 131–209, as illustrated by the red line in Figure 2.

2.2. Ancillary Data

The literature compilation of the optical and near-infrared photometry for the sample stars is given in Appendix A.

Because we use stellar atmosphere models to measure extinction curves (§3), the result will be curves that are a combination of MW foreground and SMC internal dust. Thus, we need to correct for the MW foreground dust extinction to isolate the SMC dust extinction curves. The amount of MW foreground dust can be estimated based on radio H I measurements integrated over MW velocities along each of our sightlines. Such measurements are available with a spatial resolution of $16'$ (McClure-Griffiths et al. 2009; Kalberla et al. 2010; Kalberla & Haud 2015). These measurements are given in Table 3 for all our sightlines where $N_{MW}(HI)$ is determined by integrating the velocity resolved spectrum over the MW velocities of -70 to 70 km s $^{-1}$. The MW foreground dust column can be estimated by calculating $E(B - V)_{MW}$ using the $N_{MW}(HI)$ values and the MW high Galactic latitude measured $N(HI)/E(B - V)$ value of 8.3×10^{21} H cm $^{-2}$ mag $^{-1}$ (Liszt 2014). Note this value is higher than that measured at low Galactic latitude 5×10^{21} H cm $^{-2}$ mag $^{-1}$ (Bohlin et al. 1978; Diplas & Savage 1994; Liszt 2014).

The resulting $E(B - V)_{MW}$ are given in Table 3. The $E(B - V)_{MW}$ values range from 0.029 to 0.044 mag with an average of 0.037 ± 0.0037 mag. This is significantly lower than the earlier estimate by (Schwering & Israel 1991) ($E(B - V)_{MW} = 0.07 - 0.09$), also based on H I, but compatible with the results of (Bell et al. 2019) ($E(B - V)_{MW} = 0.034 \pm 0.011$), based on the Schlegel et al. (1998) dust maps. As will be seen in §3 the lower values produce more reasonable foreground corrected extinction curves (e.g., fewer non-physical negative 2175 Å bumps).

Table 3. Ancillary Data

Name	$N_{MW}(HI)$ [10^{20} cm $^{-2}$]	$E(B - V)_{MW}$ [mag]	q_{PAH} [%]
2dFS 413	3.224 ± 0.079	0.039 ± 0.0010	0.53 ± 0.40
2dFS 626	3.183 ± 0.087	0.038 ± 0.0010	0.87 ± 0.21
2dFS 662	3.179 ± 0.060	0.038 ± 0.0007	1.01 ± 0.26
2dFS 699	3.528 ± 0.045	0.043 ± 0.0005	0.52 ± 0.45
2dFS 3014	2.492 ± 0.035	0.030 ± 0.0004	0.32 ± 0.14
2dFS 3030	2.367 ± 0.069	0.029 ± 0.0008	0.86 ± 0.21
2dFS 3171	2.368 ± 0.063	0.029 ± 0.0008	1.09 ± 0.19
AzV 4	3.499 ± 0.035	0.042 ± 0.0004	1.87 ± 1.49
AzV 18	3.179 ± 0.087	0.038 ± 0.0010	0.57 ± 0.19
AzV 23	3.208 ± 0.064	0.039 ± 0.0008	1.31 ± 0.21
AzV 70	3.621 ± 0.048	0.044 ± 0.0006	1.28 ± 0.45
AzV 86	3.156 ± 0.030	0.038 ± 0.0004	0.83 ± 0.48
AzV 132	3.134 ± 0.062	0.038 ± 0.0007	0.71 ± 0.22
AzV 214	3.019 ± 0.061	0.036 ± 0.0007	0.31 ± 0.16
AzV 218	3.175 ± 0.071	0.038 ± 0.0009	0.61 ± 0.28
AzV 289	3.021 ± 0.035	0.036 ± 0.0004	0.64 ± 0.46
AzV 380	2.576 ± 0.036	0.031 ± 0.0004	1.19 ± 0.66
AzV 398	2.911 ± 0.050	0.035 ± 0.0006	0.60 ± 0.25
AzV 456	2.666 ± 0.031	0.032 ± 0.0004	0.92 ± 0.50
AzV 462	2.766 ± 0.029	0.033 ± 0.0003	1.48 ± 0.78
BBB SMC280	3.180 ± 0.061	0.038 ± 0.0007	1.13 ± 0.19
MR12 09	3.185 ± 0.032	0.038 ± 0.0004	1.11 ± 0.18
MR12 10	3.184 ± 0.032	0.038 ± 0.0004	1.11 ± 0.18
MR12 11	3.183 ± 0.032	0.038 ± 0.0004	1.11 ± 0.18
NGC330 ELS 110	3.263 ± 0.044	0.039 ± 0.0005	1.07 ± 0.41
NGC330 ELS 114	3.250 ± 0.038	0.039 ± 0.0005	0.57 ± 0.28
NGC330 ELS 116	3.273 ± 0.046	0.039 ± 0.0006	0.92 ± 0.30
SK 191	3.437 ± 0.046	0.041 ± 0.0006	...
SMC5-398	3.343 ± 0.046	0.040 ± 0.0006	0.33 ± 0.21
SMC5-3739	3.188 ± 0.043	0.038 ± 0.0005	0.75 ± 0.17
SMC5-79264	3.208 ± 0.037	0.039 ± 0.0004	0.63 ± 0.22
SMC5-82923	3.238 ± 0.052	0.039 ± 0.0006	0.57 ± 0.42

One of the goals of this work is to compare the strength of the 2175 Å bump versus the implied dust mass fraction of PAH grains, q_{PAH} , defined as carbonaceous grains with $< 10^3$ C atoms (Draine & Li 2007), to explain the emission seen in the MIR carbonaceous features (aka PAH features). Fortunately, q_{PAH} values for the majority of our sightlines can be measured using the same data and models as used by Chastenot et al. (2019). A new q_{PAH} map was determined by fitting the Spitzer and Herschel observations at a resolution $42''$ with a data quality criteria of 1σ (instead of 3σ) in all bands. This allowed for almost all of our sightlines to be associated with a q_{PAH} measurements. The q_{PAH} values and uncertainties for our sightlines are given in Table 3.

3. EXTINCTION CURVES

In this paper, we utilize the “Extinction-Without-Standards” technique (Fitzpatrick & Massa 2005; Fitzpatrick et al. 2019) to model the observed spectral energy distribu-

tions (SEDs) of our sample of reddened stars and, ultimately, produce extinction curves covering the UV through the near-IR spectral region. In contrast to the “Pair Method” (e.g., Massa et al. 1983), which requires observations of unreddened standard stars, this technique uses stellar atmosphere calculations to represent the intrinsic SEDs of the reddened stars. This eliminates the need to observe a large grid of unreddened stars and allows the effects of mismatch between the stellar properties (e.g., T_{eff} or $\log g$) and the extinction curves to be investigated. On the other hand, it places heavy reliance on the accuracy of the atmosphere models and the absolute calibration of the observations. In addition, the Extinction-Without-Standards curves include contributions from all the dust in their respective sightlines - in this case, the Milky Way foreground - whereas such “contamination” would be largely removed by the Pair Method. This drawback is outweighed by elimination of standard star observations and also offers the opportunity to investigate the extinction properties of the foreground dust.

3.1. SED Modeling

As described in detail by Fitzpatrick & Massa (2005); Fitzpatrick et al. (2019), Extinction-Without-Standards is a modeling process in which the observed UV through near-IR SEDs of the reddened stars are fit with a combination of a stellar atmosphere model, interstellar H I Ly α absorption and a parameterized representation of the wavelength dependence of the total sightline extinction. As in Fitzpatrick et al. (2019), the principal goal of the modeling is to utilize the full range of available spectral information to determine the stellar properties and thus the intrinsic SED. The actual extinction curves are derived from normalized ratio of the observed and intrinsic SEDs, analogously to the Pair Method.

In this study, we utilized the O and B star TLUSTY non-Local Thermodynamic Equilibrium (nLTE) atmosphere grids (Lanz & Hubeny 2003, 2007) for all of our targets except MR12 10, whose T_{eff} is below the lower limit of the nLTE TLUSTY grid of 15000 K. For this star, we used the BOSZ LTE models (Bohlin et al. 2017). TLUSTY models are strongly preferred for stars with $T_{\text{eff}} \geq 15000$ K as accounting for nLTE effects are important for accurate predictions of their spectra. The interstellar Lyman α profile was taken from Bohlin (1975). The wavelength dependence of the extinction was represented in the optical and near-IR ($\lambda > 4000$ Å) using the extinction curve of Fitzpatrick et al. (2019) and in the UV ($\lambda < 2700$ Å) with the fitting function of Fitzpatrick & Massa (2007). These two pieces of the overall curve were joined together by a cubic spline interpolation. The determination of the best-fit model proceeded as follows: initial estimates of the various parameters were used to produce a high resolution model of the reddened star’s SED. In the UV, the model was then convolved with the appropriate instrumental line spread function (i.e., STIS or IUE) and binned to match the observed data. In the optical and near-IR, synthetic photometry was performed on the

bandpasses available for the star (see Appendix A). A value of χ^2 was computed, characterizing the goodness of the fit. The various parameters were then iteratively adjusted to arrive at the best possible fit to the data, as indicated by the χ^2 value. The iteration and minimization were managed by the gradient-search algorithm MPFIT written in the Interactive Data Language (IDL) by C. Markwardt¹.

The typical SED fits required the determination of 15 free parameters. These included three for the stellar model (T_{eff} , $\log g$, and v_{rad}), one for Ly α profile of SMC gas ($N(HI)_{\text{SMC}}$), and 10 for the extinction curve. The extinction curve parameters are $E(44 - 55)$ and $R(55)$ to specify the optical/NIR portion, the seven FM07 parameters to specify the UV portion, and a floating spline anchor point at 3000 Å to facilitate the joining of the UV and optical. Note that $E(55 - 44) \sim E(B - V)$ and $R(55) \sim R(V)$ (Fitzpatrick et al. 2019) and we use the more common $E(B - V)$ and $R(V)$ throughout this paper. In addition, a single scale factor is determined, to align the models with the observations at a wavelength of 5500 Å. In addition to these 15 free parameters, there are number of fixed parameters. Due to the relatively low spectral resolution of the spectrophotometry, we assumed a stellar metallicity of $[m/H] = -0.7$ and a rotational velocity of $v \sin i = 100$ km s⁻¹ for all the fits. The values of the microturbulence (either 2 km s⁻¹ or 10 km s⁻¹) were determined by the appropriate model grid. We also assumed that the MW foreground interstellar H I component is located at 0 km s⁻¹ with $N_{\text{MW}}(HI) = 3.5 \times 10^{20}$ H cm⁻² and that the SMC component is located at 120 km s⁻¹. Finally, the line-spread functions for the spectrophotometric observations were taken as Gaussians with FWHM values of 1.2 Å for STIS/G140M, 3.2 Å for STIS/G230M, and 5.5 Å for IUE.

The best fit values for the total reddening toward each star (i.e, MW plus SMC) and the stellar parameters T_{eff} and $\log g$ are given in Table 4, along with the specific model grid used. In some cases, there was insufficient information to determine definitive values of $\log g$. This usually occurs for the higher gravity stars, in which the Balmer continuum – the main gravity indicator in these fits – is less sensitive to $\log g$. In these cases, we fixed the gravity to a value of $\log g = 4.3$. Although we also fit for values of v_{rad} for each star, the low spectral resolution coupled with uncertainties in the wavelength calibration zero points render these values of little interest. The parameters describing the shape of the total UV through near-IR extinction curves are discarded at this point, as their sole purpose was to facilitate the SED modeling. The actual extinction curves analyzed below are created by ratioing the observed and best-fit intrinsic SEDs and normalizing by the appropriate value of $E(B - V)$.

3.2. MW Foreground Correction

Extinction curves produced from the ratio of the intrinsic SEDs derived above and the observed SMC SEDs con-

¹ <https://pages.physics.wisc.edu/~craigm/idl/fitting.html>

Table 4. Stellar Fit Parameters

Name	$E(B - V)_{\text{MW+SMC}}$	T_{eff} [K]	$\log g$	Model Grid ^a
2dFS 413	0.200 ± 0.025	19172 ± 1060	3.186 ± 0.406	TLUB2
2dFS 626	0.247 ± 0.021	23518 ± 998	4.3^b	TLUB2
2dFS 662	0.237 ± 0.018	26919 ± 416	4.3^b	TLUB2
2dFS 699	0.184 ± 0.020	15216 ± 554	2.232 ± 0.255	TLUB2
2dFS 3014	0.236 ± 0.024	25953 ± 765	4.3^b	TLUB2
2dFS 3030	0.287 ± 0.024	36226 ± 301	4.3^b	TLUO10
2dFS 3171	0.400 ± 0.019	35412 ± 929	4.3^b	TLUO10
AzV 4	0.315 ± 0.006	24156 ± 249	2.766 ± 0.049	TLUB10
AzV 18	0.202 ± 0.011	19636 ± 326	2.335 ± 0.081	TLUB10
AzV 23	0.249 ± 0.008	18076 ± 395	3.090 ± 0.137	TLUB10
AzV 70	0.099 ± 0.015	30414 ± 547	3.379 ± 0.099	TLUO10
AzV 86	0.122 ± 0.014	28774 ± 148	4.3^b	TLUO10
AzV 132	0.385 ± 0.016	33343 ± 172	4.3^b	TLUO10
AzV 214	0.232 ± 0.014	22452 ± 775	2.660 ± 0.167	TLUB10
AzV 218	0.163 ± 0.017	24212 ± 300	2.982 ± 0.077	TLUB10
AzV 289	0.114 ± 0.016	28193 ± 726	3.111 ± 0.127	TLUO10
AzV 380	0.090 ± 0.016	21834 ± 544	2.554 ± 0.127	TLUB10
AzV 398	0.322 ± 0.021	30229 ± 1329	3.031 ± 0.156	TLUO10
AzV 456	0.387 ± 0.011	34525 ± 845	4.3^b	TLUO10
AzV 462	0.051 ± 0.022	20705 ± 384	2.497 ± 0.140	TLUB10
BBB SMC280	0.193 ± 0.018	22773 ± 1843	2.990 ± 0.705	TLUB2
MR12 09	0.133 ± 0.005	15886 ± 300	4.3^b	TLUB2
MR12 10	0.249 ± 0.010	14465 ± 500	4.3^b	BOSZ
MR12 11	0.309 ± 0.008	20410 ± 400	4.3^b	TLUB2
NGC330 ELS 110	0.093 ± 0.007	26247 ± 520	4.3^b	TLUB2
NGC330 ELS 114	0.097 ± 0.012	24051 ± 599	4.3^b	TLUB2
NGC330 ELS 116	0.080 ± 0.009	20899 ± 495	4.3^b	TLUB2
SK 191	0.119 ± 0.019	19863 ± 307	2.270 ± 0.095	TLUB10
SMC5-398	0.147 ± 0.011	16790 ± 279	4.3^b	TLUB2
SMC5-3739	0.141 ± 0.011	15964 ± 411	3.474 ± 0.241	TLUB2
SMC5-79264	0.231 ± 0.017	17505 ± 470	4.220 ± 0.361	TLUB2
SMC5-82923	0.129 ± 0.020	16410 ± 372	3.714 ± 0.216	TLUB2

^aThis column indicates the model atmosphere grid used to compute the intrinsic SED each star. “TLUO10” refers to the nLTE O star grid of Lanz & Hubeny (2003), computed with a value of $v_{\text{turb}} = 10 \text{ km s}^{-1}$. “TLUB2” and “TLUB10” refer to the B star grids from Lanz & Hubeny (2007), computed with $v_{\text{turb}} = 2 \text{ km s}^{-1}$ and 10 km s^{-1} , respectively. In the T_{eff} and $\log g$ region where these models overlap, the model which provided the best fit to the data was adopted. “BOSZ” refers to LTE grid of Bohlin et al. (2017), computed with $v_{\text{turb}} = 2 \text{ km s}^{-1}$. These models were used for the one star with $T_{\text{eff}} \leq 15000 \text{ K}$.

^b $\log g$ fixed due to insufficient spectral information.

tain contributions from the SMC internal dust and MW foreground dust. For this paper we focus on the properties of SMC dust and so need to correct for the MW foreground extinction. This correction was done by subtracting a model of the MW foreground extinction from the measured total extinction curve. The model used was the MW average curve corresponding to the Galactic average value of $R(V) = 3.1$ (Gordon et al. 2023) and the appropriate MW foreground reddening ($E(B - V)_{\text{MW}}$; see Table 3). To the extent that the wavelength dependence of the foreground extinction can rep-

resented by the $R(V) = 3.1$ curve, the result will be SMC-only extinction curves. The normalization values for the resulting SMC only curves, $E(B - V)_{\text{SMC}}$, are determined by subtracting the $E(B - V)_{\text{MW}}$ values in Table 3 from the total $E(B - V)_{\text{MW+SMC}}$ values in Table 4. While little is known of the true wavelength dependence of MW extinction extinction along high latitude sightlines, the success of this model indicates that it is likely similar to MW average. In future work, we plan to investigate the MW foreground extinction

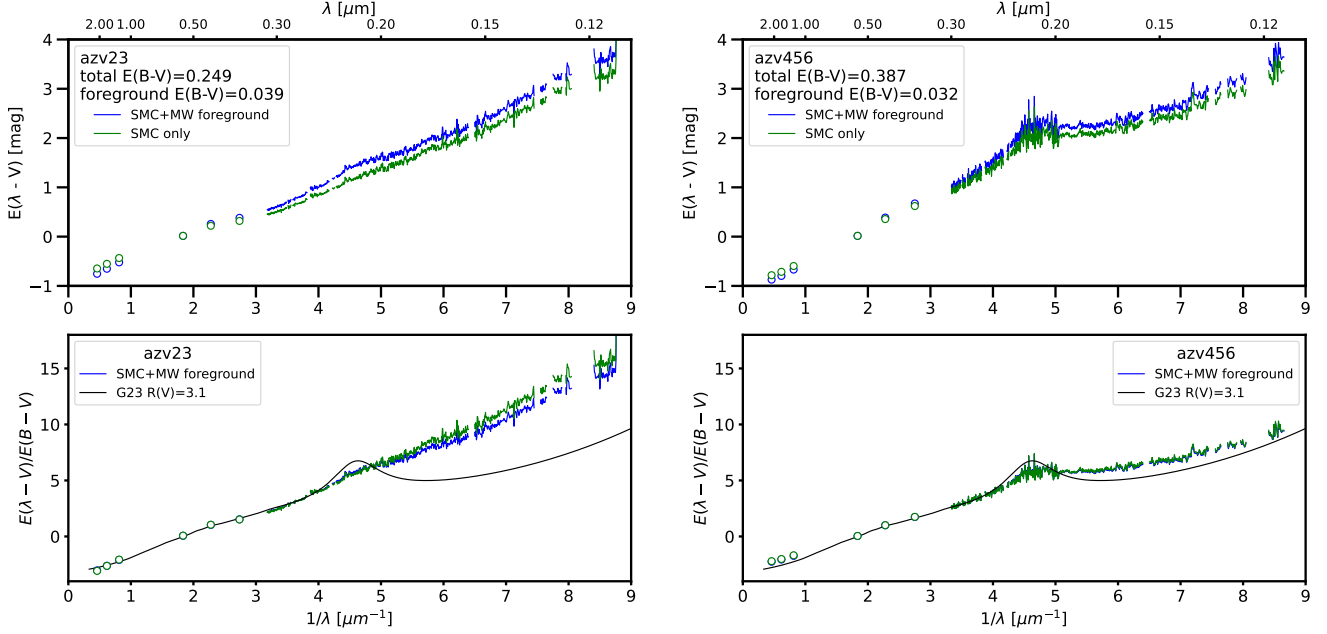


Figure 3. The as measured (SMC+MW) and after MW foreground corrected (SMC only) extinction curves are shown and illustrate the importance of the foreground correction. The upper plots give the as measured extinction curves and the bottom plots the normalized extinction curves. The foreground correction is small, but significant especially for AzV 23 where the very weak 2175 Å bump is seen to be due to MW foreground dust. The curves are plotted versus $1/\lambda$ as this is common for UV extinction studies and it is particularly useful as the majority of the SMC sightlines are roughly linear with $1/\lambda$.

along Magellanic Cloud sightlines using observations of the most lightly reddened stars in the SMC and LMC.

The effect of the MW foreground correction is illustrated in Fig. 3 for two sightlines. The first sightline, towards AzV 23, shows a weak 2175 Å in the measured MW+SMC extinction curve, which is eliminated once the MW foreground is removed. This behavior is seen for many of our sightlines, i.e., weak 2175 Å signatures that disappear once the MW foreground is removed. This suggests the our assumed form for the MW foreground extinction curve does not overestimate the normalized strength of the 2175 Å bump, otherwise the corrected curves would show dips at 2175 Å. The behavior for the AzV 23 curve is in contrast to the sightline towards AzV 456 where the MW foreground correction changes the normalized extinction curve very little. This is not surprising as the assumed MW foreground extinction curve is similar to the combined MW+SMC extinction curve for this sightline.

3.3. The SMC Extinction Curves

The MW foreground-corrected extinction curves for the sample of 32 stars are shown in Fig. 4. The curves have been grouped based on their $E(B - V)_{\text{SMC}}$ values and shapes. The groups are:

1. $E(B - V)_{\text{SMC}} > 0.1$, steep UV extinction rising linearly to shorter wavelengths, and weak/absent 2175 Å bumps ($B_3 < 3\sigma$ or negative),
2. $E(B - V)_{\text{SMC}} > 0.1$ and significant 2175 Å bumps ($B_3 > 3\sigma$)
3. $E(B - V)_{\text{SMC}} > 0.1$, fairly flat UV extinction, and weak/absent 2175 Å bumps
4. $E(B - V)_{\text{SMC}} < 0.1$ with dust columns are low enough to be significantly impacted by uncertainties in the MW foreground correction and the measured $E(B - V)_{\text{SMC}}$.

The first group shows behaviors similar to those labeled “SMC Bar” by Gordon et al. (2003). The second group includes all the known sightlines with a 2175 Å bump including AzV 456. The third group includes two sightlines that display fairly flat UV extinction and this is a behavior that is usually associated with sightlines lacking many small grains (Whittet et al. 2004). Such a behavior could also be the result of over-estimating the $E(B - V)_{\text{SMC}}$ dust column or a significant mismatch between the observed and model stellar parameters. We consider these two sightlines to be intriguing, but more work would be needed to confirm them. The fourth group curves are generally noisier and have larger uncertainties on their overall slopes (e.g., C_2 values) and some display negative 2175 Å bumps with this latter property being highly unlikely given our understanding of this feature

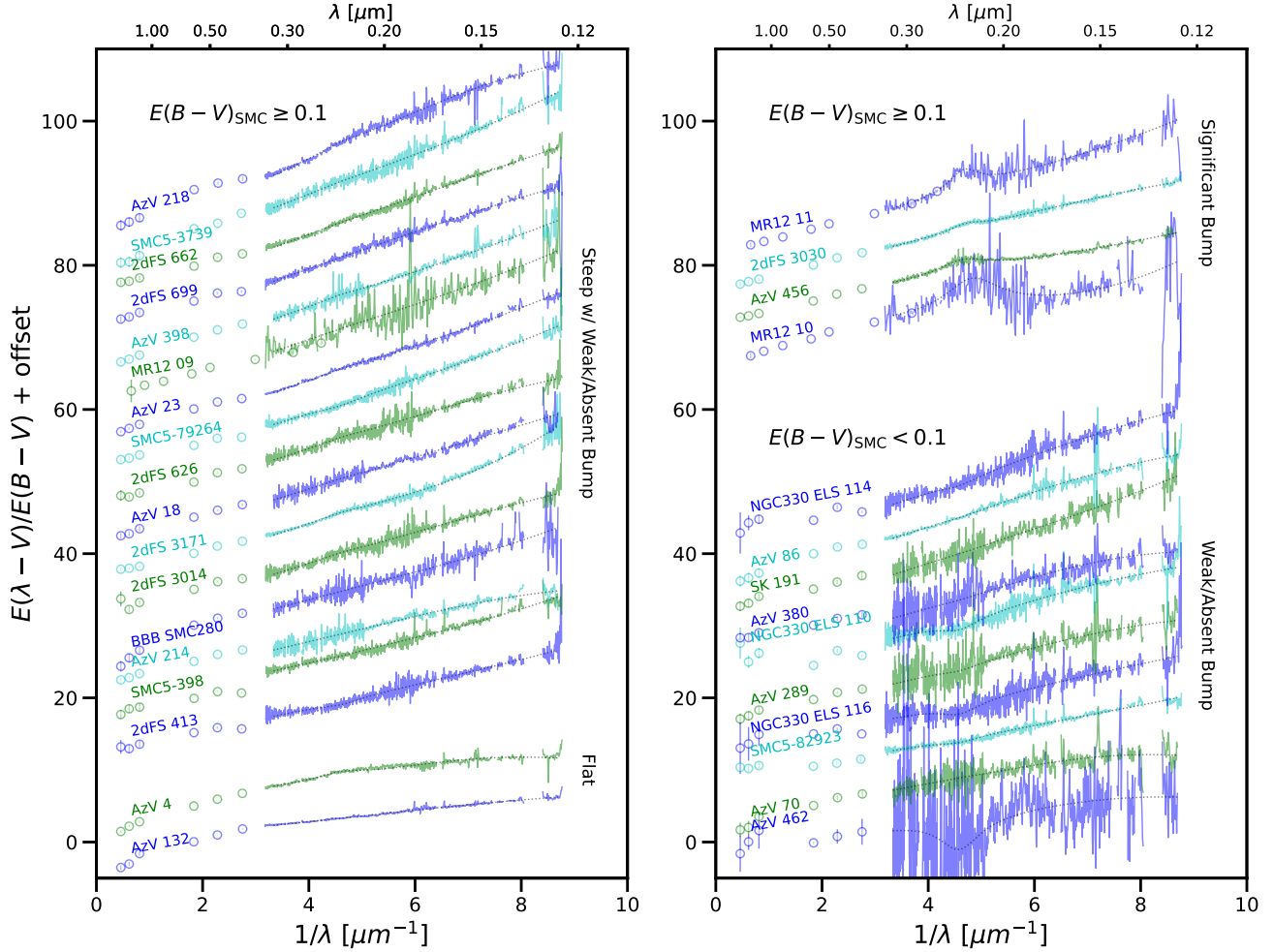


Figure 4. The MW foreground corrected SMC only extinction curves are plotted along with the FM90 fits for the UV portion (dotted lines). For clarity, the curves have been offset on the y-axis by multiples of 5. For ease of interpretation the top axis labels provide representative values in λ units. Regions of strong residuals due to stellar or interstellar gas lines have been masked. The extinction curves are grouped based on their observed behavior and $E(B - V)_{\text{SMC}}$ values. Inside of each group, the curves are displayed from flattest to steepest based on the fitted FM90 C_2 values.

(e.g., Calzetti et al. 1995). The fourth group is included for completeness, but will not be included in any of the analysis done in this paper.

The gas columns, dust columns, and FM90 parameters for the UV portions of the extinction curves are given in Tables 5 and 6. In addition, average values are provided for the first and second groups. The dust and gas columns for each extinction curve are quantified by $E(B - V)_{\text{SMC}}$, $A(V)_{\text{SMC}}$, and $N(HI)_{\text{SMC}}$. The $E(B - V)_{\text{SMC}}$ were determined by subtracting the MW foreground reddenings in Table 3 from the total reddenings in Table 4 that resulted from the fitting procedure. The $A(V)_{\text{SMC}}$ values were determined by comparing the NIR $E(\lambda - V)_{\text{SMC}}$ extinction to the $A(\lambda)/A(V)$ average from Declair et al. (2022) following the Gordon et al. (2003) method updated for $A(V)$ instead of $R(V)$, as motivated by Gordon et al. (2009). Similar $A(V)$ values are found using the Rieke et al. (1989) average as the comparison in-

stead. The $R(V)_{\text{SMC}}$ values, which probe the average dust grain size, are $A(V)_{\text{SMC}}/E(B - V)_{\text{SMC}}$. The $N(HI)_{\text{SMC}}$ were determined from the fitting procedure with a small additional correction. The modeling process assumed a uniform MW foreground component of $3.5 \times 10^{20} \text{ H cm}^{-2}$ for all stars and attributed any excess absorption in the Lyman α line to SMC gas. We corrected this result for the small difference between the assumed MW foreground column and that inferred from the 21-cm emission (Table 3).

To quantify the properties of the UV portion of each foreground-corrected curve, we fit them with the FM90 parameters, but with the 2175 Å bump strength given by $B_3 \equiv C_3/\gamma^2$ instead of C_3 as in FM90. B_3 is a direct measure of the 2175 Å bump amplitude and is much less correlated with γ than C_3 . Given the weakness/absence of the 2175 Å bump in most of the sightlines, the 2175 Å bump center and width were fixed for all sightlines to the MW average val-

Table 5. Extinction Parameters

Name	$E(B - V)_{\text{SMC}}$	$A(V)_{\text{SMC}}$	$R(V)_{\text{SMC}}$	$N(HI)_{\text{SMC}}$	C_1	C_2	B_3	C_4
	[mag]	[mag]		[10^{21} H cm $^{-2}$]				
$E(B - V)_{\text{SMC}} \geq 0.1$, Steep with Weak/Absent Bump								
2dFS 413	0.16 ± 0.03	0.35 ± 0.07	2.17 ± 0.54	8.17 ± 0.72	-2.78 ± 0.15	1.61 ± 0.05	-0.61 ± 0.24	0.08 ± 0.03
2dFS 626	0.21 ± 0.03	0.49 ± 0.06	2.35 ± 0.37	16.63 ± 1.01	-4.30 ± 0.21	2.22 ± 0.07	0.18 ± 0.17	-0.13 ± 0.04
2dFS 662	0.20 ± 0.02	0.51 ± 0.05	2.56 ± 0.34	13.46 ± 0.40	-6.03 ± 0.21	2.59 ± 0.06	0.04 ± 0.13	-0.02 ± 0.02
2dFS 699	0.14 ± 0.02	0.36 ± 0.03	2.52 ± 0.42	13.09 ± 0.47	-5.73 ± 0.20	2.56 ± 0.07	0.07 ± 0.13	-0.11 ± 0.03
2dFS 3014	0.21 ± 0.02	0.55 ± 0.05	2.68 ± 0.37	12.78 ± 0.42	-4.96 ± 0.13	2.15 ± 0.03	0.15 ± 0.09	-0.08 ± 0.03
2dFS 3171	0.37 ± 0.02	0.90 ± 0.04	2.42 ± 0.16	9.55 ± 1.18	-4.62 ± 0.10	2.18 ± 0.03	0.27 ± 0.07	0.62 ± 0.02
AzV 18	0.16 ± 0.02	0.42 ± 0.06	2.58 ± 0.37	10.06 ± 1.13	-4.87 ± 0.31	2.21 ± 0.09	0.13 ± 0.22	0.01 ± 0.04
AzV 23	0.21 ± 0.01	0.67 ± 0.03	3.17 ± 0.21	8.90 ± 0.48	-5.69 ± 0.19	2.41 ± 0.06	0.25 ± 0.12	0.16 ± 0.02
AzV 214	0.20 ± 0.02	0.51 ± 0.03	2.59 ± 0.25	5.52 ± 0.61	-4.19 ± 0.20	1.76 ± 0.04	-0.05 ± 0.16	-0.23 ± 0.03
AzV 218	0.12 ± 0.02	0.60 ± 0.04	4.83 ± 0.80	4.67 ± 0.18	-8.36 ± 0.54	3.27 ± 0.17	0.43 ± 0.21	-0.41 ± 0.06
AzV 398	0.29 ± 0.02	1.03 ± 0.03	3.59 ± 0.21	11.13 ± 2.39	-5.54 ± 0.16	2.44 ± 0.04	0.19 ± 0.11	0.09 ± 0.03
BBB SMC280	0.15 ± 0.02	0.87 ± 0.04	5.61 ± 0.74	7.62 ± 1.83	-4.10 ± 0.24	1.92 ± 0.06	0.02 ± 0.19	0.18 ± 0.06
MR12 09	0.09 ± 0.01	0.28 ± 0.18	2.92 ± 1.90	8.31 ± 1.22	-4.95 ± 0.53	2.41 ± 0.11	0.02 ± 0.38	0.19 ± 0.14
SMC5-398	0.11 ± 0.01	0.22 ± 0.05	2.08 ± 0.49	0.48 ± 0.11	-1.99 ± 0.10	1.73 ± 0.05	-0.18 ± 0.19	0.18 ± 0.03
SMC5-3739	0.10 ± 0.01	0.53 ± 0.05	5.20 ± 0.66	4.50 ± 0.21	-6.32 ± 0.31	2.78 ± 0.10	0.16 ± 0.17	0.22 ± 0.04
SMC5-79264	0.19 ± 0.02	0.39 ± 0.03	2.00 ± 0.24	11.20 ± 0.55	-4.82 ± 0.11	2.35 ± 0.04	-0.51 ± 0.10	0.17 ± 0.02
SMC Average	3.02 ± 0.18	...	-5.07 ± 0.05	2.30 ± 0.01	0.12 ± 0.03	0.07 ± 0.02
$E(B - V)_{\text{SMC}} \geq 0.1$, Significant Bump								
2dFS 3030	0.26 ± 0.03	0.70 ± 0.04	2.72 ± 0.30	11.84 ± 0.27	-3.38 ± 0.10	1.79 ± 0.03	0.79 ± 0.08	-0.11 ± 0.02
AzV 456	0.35 ± 0.01	0.85 ± 0.02	2.39 ± 0.10	1.31 ± 0.22	-1.76 ± 0.09	1.23 ± 0.01	1.81 ± 0.04	0.11 ± 0.01
MR12 10	0.21 ± 0.01	0.65 ± 0.09	3.08 ± 0.45	36.17 ± 16.54	-0.02 ± 0.56	0.79 ± 0.10	4.52 ± 0.39	0.63 ± 0.15
MR12 11	0.27 ± 0.01	0.71 ± 0.10	2.61 ± 0.37	10.10 ± 2.59	-4.09 ± 0.26	2.07 ± 0.05	2.68 ± 0.19	0.23 ± 0.08
SMC Bumps	2.55 ± 0.10	...	-2.85 ± 0.21	1.51 ± 0.04	2.64 ± 0.12	0.25 ± 0.06
$E(B - V)_{\text{SMC}} \geq 0.1$, Flat								
AzV 4	0.27 ± 0.01	0.95 ± 0.03	3.47 ± 0.13	0.58 ± 0.08	-1.01 ± 0.04	1.11 ± 0.01	0.74 ± 0.05	-0.37 ± 0.02
AzV 132	0.35 ± 0.02	1.17 ± 0.07	3.38 ± 0.25	6.60 ± 0.18	-0.21 ± 0.02	0.77 ± 0.00	-0.05 ± 0.07	-0.04 ± 0.01
$E(B - V)_{\text{SMC}} < 0.1$, Weak/Absent Bump								
AzV 70	0.06 ± 0.02	0.18 ± 0.03	3.20 ± 1.00	0.90 ± 0.20	-2.50 ± 0.31	1.35 ± 0.07	0.25 ± 0.37	-0.42 ± 0.10
AzV 86	0.08 ± 0.01	0.34 ± 0.03	4.01 ± 0.75	0.06 ± 0.05	-5.89 ± 0.23	2.42 ± 0.07	-0.26 ± 0.16	-0.28 ± 0.04
AzV 289	0.08 ± 0.02	0.22 ± 0.03	2.86 ± 0.69	3.20 ± 0.23	-3.42 ± 0.41	1.75 ± 0.08	-0.79 ± 0.33	-0.16 ± 0.06
AzV 380	0.06 ± 0.02	0.11 ± 0.02	1.83 ± 0.60	3.37 ± 0.62	-5.03 ± 0.50	1.95 ± 0.10	-0.24 ± 0.37	-0.28 ± 0.07
AzV 462	0.02 ± 0.02	0.00 ± 0.02	0.06 ± 1.28	0.07 ± 0.04	0.49 ± 1.43	0.81 ± 0.21	-4.73 ± 1.88	-0.22 ± 0.21
NGC330 ELS 110	0.05 ± 0.01	-0.05 ± 0.04	-1.00 ± 0.86	3.76 ± 0.15	-3.09 ± 0.28	1.97 ± 0.11	-1.52 ± 0.49	-0.16 ± 0.07
NGC330 ELS 114	0.06 ± 0.01	0.03 ± 0.04	0.57 ± 0.76	5.51 ± 0.21	-6.24 ± 0.47	2.50 ± 0.13	-0.84 ± 0.35	-0.11 ± 0.06
NGC330 ELS 116	0.04 ± 0.01	0.04 ± 0.07	0.92 ± 1.68	1.98 ± 0.13	-2.85 ± 0.36	1.58 ± 0.10	-1.71 ± 0.72	-0.02 ± 0.07
SK 191	0.08 ± 0.02	0.16 ± 0.03	2.12 ± 0.63	3.08 ± 0.40	-5.62 ± 0.44	2.35 ± 0.12	-0.25 ± 0.31	0.18 ± 0.05
SMC5-82923	0.09 ± 0.02	-0.04 ± 0.04	-0.49 ± 0.47	3.90 ± 0.20	-1.56 ± 0.08	1.30 ± 0.03	-0.64 ± 0.28	0.05 ± 0.03

ues of $4.59 \mu\text{m}^{-1}$ and $0.95 \mu\text{m}$, respectively (Valencic et al. 2004; Fitzpatrick & Massa 2007; Gordon et al. 2009), except for those with significant bumps. The FM90 fit uncertainties were determined by calculating the best fit, empirically determining the uncertainties from the differences between the observations and the best fit, and then using the “emcee” MCMC sampling package (Foreman-Mackey et al. 2013) with 5000 samples discarding the first 1000 samples. The uncertainties include accounting for the foreground uncertainties based on repeating the fitting with $E(B - V)_{\text{MW}}$ plus and minus the uncertainties given in Table 3 and adding the resulting uncertainties in quadrature.

3.4. Comparison to Previous Work

Eight of the sightlines measured in this work have also been measured previously and the comparisons to them are

shown in Fig. 5. The five sightlines towards AzV stars were measured by Gordon et al. (2003) using the standard pair method where the comparisons used were *observed* spectra of SMC stars with low reddening, implicitly correcting for MW foreground dust. Our new and the previous curves for these five sightlines are very similar providing validation of the foreground extinction correction for the new measurements.

The comparisons for the three sightlines towards the MR12 stars as measured by Maíz Apellániz & Rubio (2012) show significant differences. These previous extinction curves were measured for the total MW+SMC dust column and hence for these comparisons we show our MW+SMC extinction curves. The largest differences are seen in the FUV where the previous measurements were based on a single photometric measurement. In the NUV where the previous

Table 6. Detailed Bump Parameters^a

Name	x_o [μm^{-1}]	γ [μm^{-1}]
2dFS 3030	4.71 ± 0.02	0.72 ± 0.05
AzV 456	4.69 ± 0.01	1.42 ± 0.07
MR12 10	4.83 ± 0.04	1.20 ± 0.22
MR12 11	4.68 ± 0.03	0.73 ± 0.10
SMC Bumps	4.73 ± 0.03	1.15 ± 0.14

^aFor all other sightlines, these parameters were fixed to the average MW values of $x_o = 4.59 \mu\text{m}^{-1}$ and $\gamma = 0.95 \mu\text{m}^{-1}$.

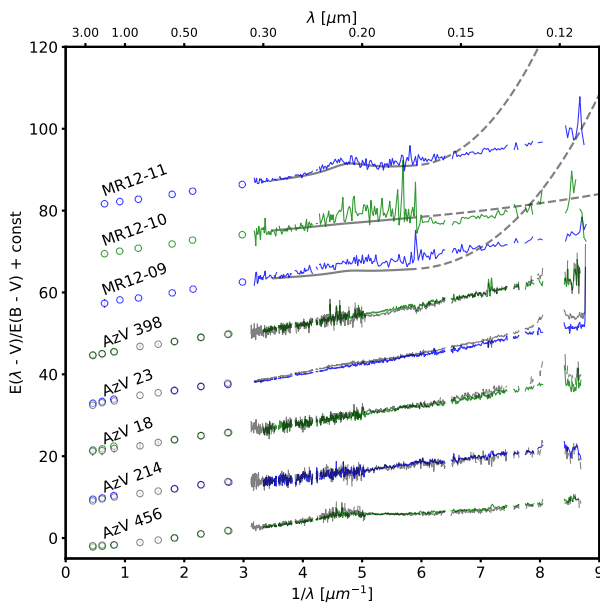


Figure 5. The comparison of the MW foreground corrected (blue/green lines) and previous literature (gray lines) extinction curves are shown. Note that some of the curves overlap so well that it is hard to see both curves. The five AzV sightlines show the comparison with the [Gordon et al. \(2003\)](#) sample and the three MR12 sightlines show the comparison with the [Maíz Apellániz & Rubio \(2012\)](#) sample based on their [Fitzpatrick & Massa \(1990\)](#) parameters. For the MR12 sample, the solid lines show the region based on spectroscopy and the dashed line the region based on a single far-UV photometric measurement. The new extinction curves agree well for the [Gordon et al. \(2003\)](#) sample, but can be significantly different for the MR12 sample.

measurements were based on UV prism spectroscopy, the comparisons is quite good for MR12 11, but shows significant differences for the other two stars. For MR12 09, our measurements show a stronger linear rise with decreasing wavelength. For MR12 10, our measurements show a marked difference, displaying a significant 2175 Å bump and far-UV curvature where the previously measured extinction curve exhibits only a linear component. One possible explanation of the difference may be the challenges of the quite low resolution UV prism data in comparison to the new higher resolution slit spectroscopy.

4. SMC PROPERTIES

4.1. Environmental Dependence

[Gordon & Clayton \(1998\)](#) speculated that nearby star formation was the cause of the bumpless sightlines seen towards some SMC stars. This was suggested by the apparent association of the star-forming SMC Bar with the bumpless sightlines and the more quiescent SMC Wing with the one then-known sightline with a bump. Based on only four sightlines, this simple picture was challenged by the finding of two sightlines with and two sightlines without bumps very near each other ($\sim 10''$) in a small region in the SMC Bar by ([Maíz Apellániz & Rubio 2012](#)).

Using our larger sample, the dependence of the dust extinction properties on environmental factors can be investigated in more detail by examining the locations of the sightlines on a representative SMC image. This is done in Fig. 6 where the sightline positions are superimposed on the SMC MIPS 24 μm image ([Gordon et al. 2014](#)), with different symbols for the four different types of curves. The 24 μm emission traces embedded star formation, and effectively represents the combination of star formation and dust. It is clear from the image that sightlines both with and without 2175 Å bumps are found throughout the SMC, including the Bar and Wing, and have no clear general association with 24 μm emission. In addition, the two zoomed images in Fig. 6 show that there are sightlines with and without 2175 Å bumps in close proximity as projected on the sky. This was initially discovered by [Maíz Apellániz & Rubio \(2012\)](#) and strengthened by our finding of a second region in the SMC Wing showing similar spatial variations.

Given the behavior of this larger sample, it is certainly not clear whether nearby star formation is an important factor in the determination of extinction curve properties. While the simple 2D positional analysis could be compromised by the line-of-sight depth of the SMC, it may also be that other factors play significant roles. For example, dust self-shielding could explain why dust producing significant 2175 Å bumps can be found near regions of star formation. Evidence that this might play a role can be seen in the behavior of LMC dust extinction, where stronger 2175 Å bumps are found near the 30 Dor star-forming region, which is associated with significant molecular material ([Misselt et al. 1999](#)).

4.2. Average Curves

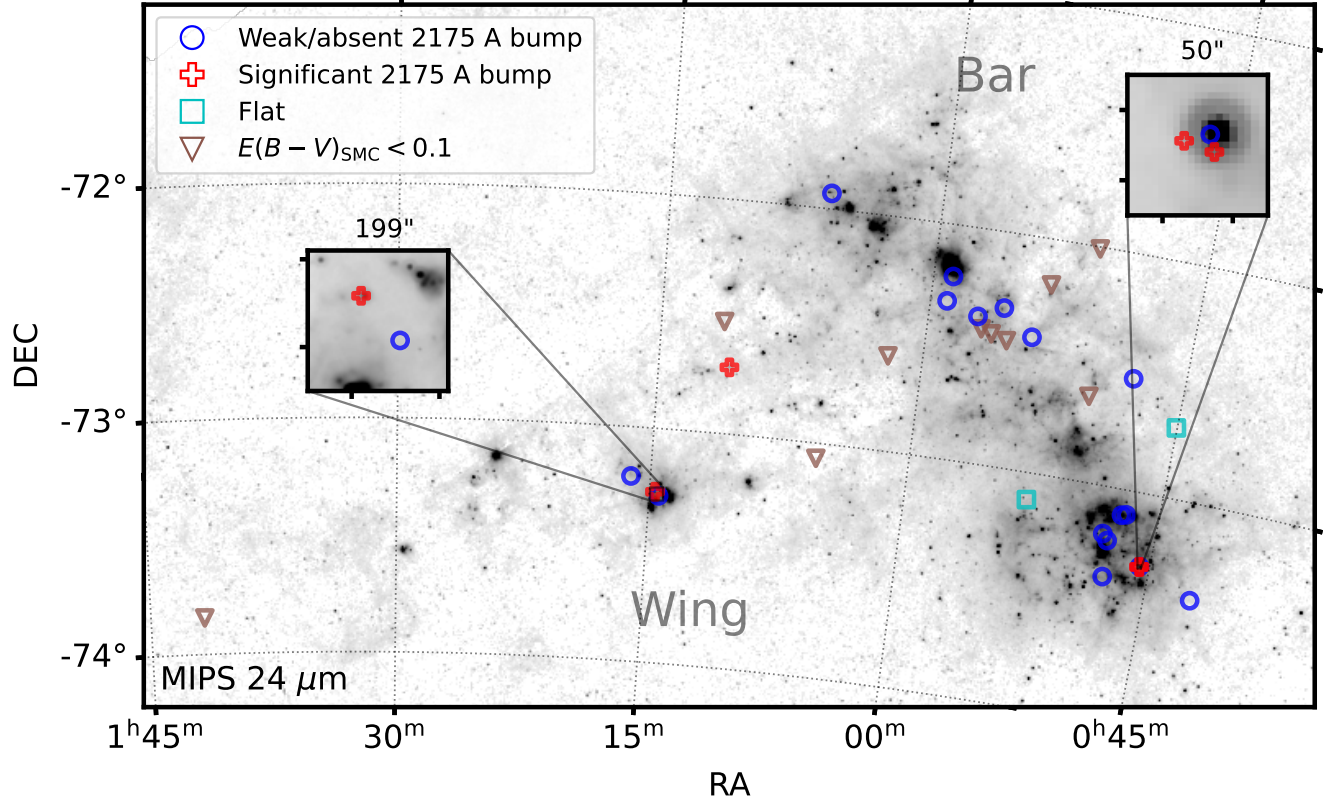


Figure 6. The locations of the extinction curve sightlines are shown on a MIPS 24 μm image. MIPS 24 μm traces the dust distribution with a focus on the youngest, embedded star formation. Zoomed images of two regions containing sightlines that probe small angular scales are shown. The different groups are shown with different symbols. The weak/absent 2175 Å bump sightlines are located throughout the galaxy including the Bar (tilted region on the right) and Wing (more diffuse region extending from the Bar towards the left). The sightlines with significant 2175 Å bumps are located in three well separated regions including in the Bar and Wing.

The averages for the two main SMC extinction samples are given in Fig. 7 and tabulated in Table 7. The $R(V)$ values and FM90 parameters for these two averages are given in Tables 5 and 6. These averages are provided as they are often used in dust grain modeling, accounting for extinction along sightlines without measured extinction curves, and comparisons to similar averages in other galaxies.

We designate the average created from the 16 sightlines in the weak/absent 2175 Å bump sample as the “SMC Average” curve. This is motivated by our finding that the extinction curves in this sample are seen throughout the SMC and include most SMC sightlines. The SMC Average curve is very similar to the “SMCBar” average curve from Gordon et al. (2003) that was determined from only four sightlines in the SMC Bar. The main difference is that the new larger sample has an average $R(V) = 3.02 \pm 0.18$, consistent with the MW average $R(V)$ whereas the SMCBar sample of Gordon et al. (2003) had an average $R(V)$ of 2.74.

The average of the four sightlines in the significant 2175 Å bump sample is designated as the “SMC Bumps” curve. This average has a weaker 2175 Å bump and lower extinction in

the near-UV than the MW $R(V) = 2.55$ average, but very similar far-UV extinction. This average is less certain as it is composed of only four sightlines and it may change significantly when a larger sample of SMC sightlines with 2175 Å bumps is available.

4.3. The 2175 Å bump and MIR Carbonaceous Features

The 2175 Å bump is most likely due to small carbonaceous grains (e.g., Mathis 1994) and the MIR carbonaceous features (aka PAH, UIR, AEF, etc. features) are definitely due to small carbonaceous grains (Duley & Williams 1981). This has led to the hypothesis that these two features are due to the same small carbonaceous grains (Draine & Li 2007). This predicts that these two features should be correlated as they are from the same grain sizes and composition. These two features are seen to be correlated in the MW for some, but not all of the MIR carbonaceous features (Massa et al. 2022). Specifically, the 6.2 μm features are not correlated with the 2175 Å bump, but three other features (7.6, 8.5, and 11.3 μm) are correlated.

We have tested this hypothesis in the SMC (and LMC) as well as currently possible in Fig. 8 where the 2175 Å bump area is plotted versus q_{PAH} , the mass fraction

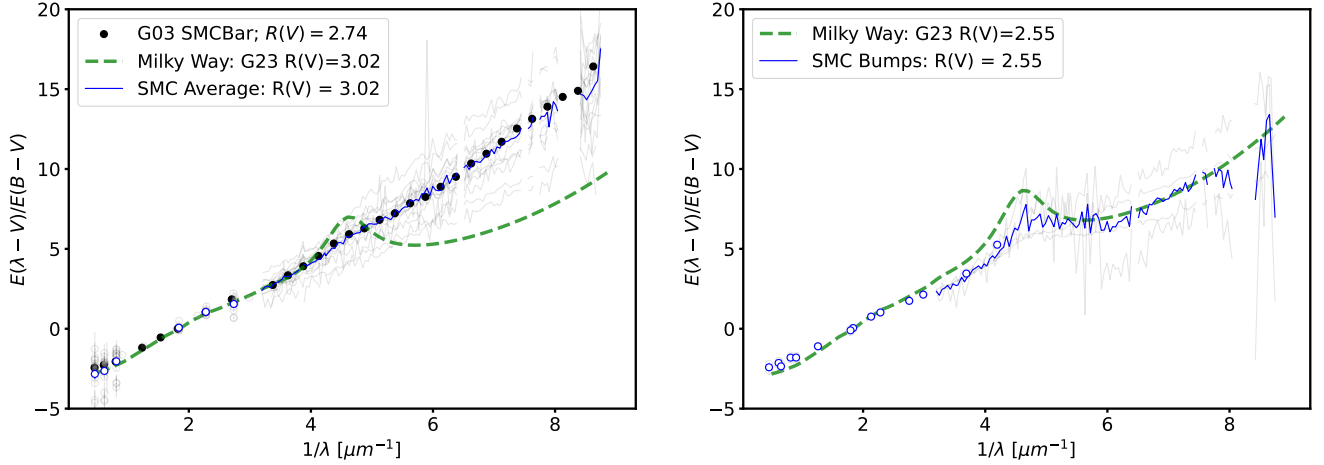


Figure 7. The average extinction curves are shown for the weak/absent 2175 Å bump (aka SMC Average) and significant bumps (aka SMC Bumps) samples. The individual curves that contributed to each average are shown in gray. These curves have been rebinned by a factor of 10. The averages were done with the $E(\lambda - V)/E(B - V)$ curves and the $R(V)$ values for these averages were computed analogous to how the $A(V)$ values were computed (see §3.3). The Gordon et al. (2003) SMC average (aka SMCBar) and MW average extinction for the same $R(V)$ as the average (Gordon et al. 2023) are shown for comparison.

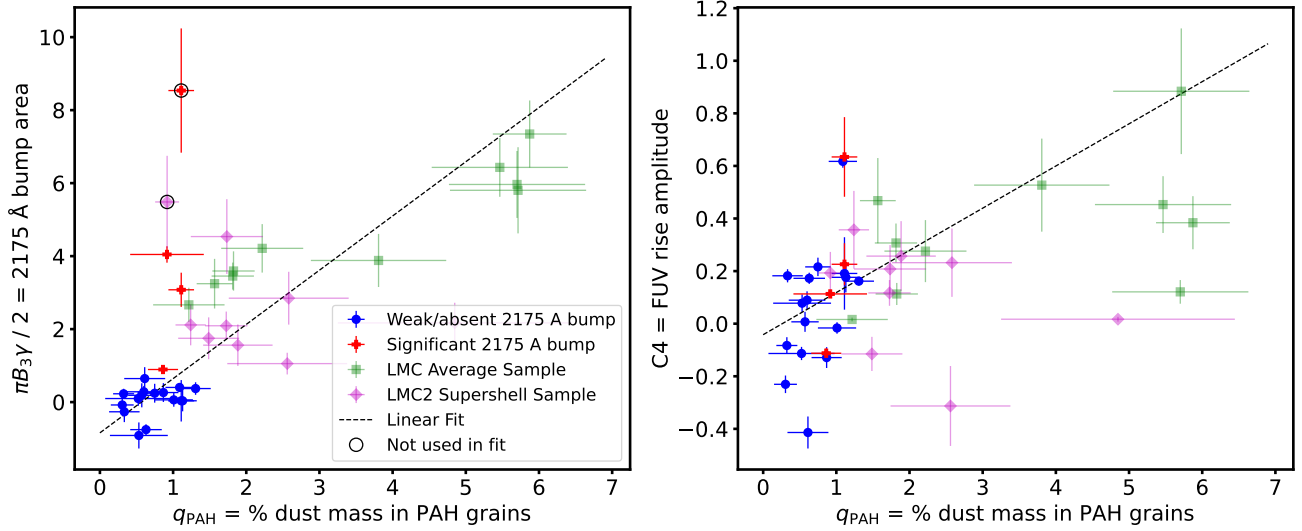


Figure 8. The area of the 2175 Å bump ($\pi B_3 \gamma / 2$) and the amplitude of the FUV rise are plotted versus the percentage mass fraction of PAH grains (q_{PAH}). q_{PAH} was derived by fitting the IR emission SED at sightline positions. The 2175 Å bump and C_4 values for the SMC extinction sightlines are from this paper and from Misselt et al. (1999) for the LMC sightlines. The q_{PAH} values for the SMC are described in §2.2 and the LMC values obtained from the same source (Chasten et al. 2019). The linear fit was determined using fitting with outlier removal and the points removed are indicated.

of “PAH” grains as compared to the total mass of dust. MW points are not included as the q_{PAH} measurements for the extinction sightlines are not available. In addition, this figure also shows the correlation with the FUV rise amplitude as it is postulated to be the wing of a carbonaceous feature peaking around ~ 715 Å (Joblin et al. 1992; Li & Draine 2001; Gordon et al. 2009). The q_{PAH} values are determined by fitting the Spitzer and Herschel observations at a resolution of

42'' (Chasten et al. 2019) and, hence, are averages around the extinction sightlines and through the entire column in the galaxy at that location. This is in contrast to the extinction measurements that are for pencil beams along the sightline towards each star. Therefore, the q_{PAH} versus 2175 Å bump area or FUV rise correlations are unlikely to be perfect as the q_{PAH} value is averaged over a larger volume than 2175 Å bump. Note that the q_{PAH} values so derived are driven by

Table 7. Sample Averages

λ	x	Band	SMC Average	SMC Bumps
[μm]	[μm^{-1}]		$A(\lambda)/A(V)$	$A(\lambda)/A(V)$
0.112	8.904	IUE/STIS	6.929 ± 0.203	4.326 ± 0.426
0.117	8.546	IUE/STIS	5.899 ± 0.036	5.480 ± 0.105
0.122	8.202	IUE/STIS	5.377 ± 0.180	4.320 ± 0.833
0.127	7.872	IUE/STIS	5.511 ± 0.031	4.806 ± 0.085
0.132	7.555	IUE/STIS	5.173 ± 0.036	4.724 ± 0.085
0.138	7.251	IUE/STIS	4.914 ± 0.023	4.444 ± 0.059
0.144	6.959	IUE/STIS	4.654 ± 0.021	4.269 ± 0.053
0.150	6.679	IUE/STIS	4.428 ± 0.021	4.048 ± 0.056
0.156	6.411	IUE/STIS	4.167 ± 0.024	3.750 ± 0.071
0.163	6.153	IUE/STIS	3.973 ± 0.019	3.689 ± 0.048
0.169	5.905	IUE/STIS	3.804 ± 0.023	3.656 ± 0.043
0.176	5.668	IUE/STIS	3.615 ± 0.018	3.563 ± 0.042
0.184	5.439	IUE/STIS	3.435 ± 0.016	3.452 ± 0.030
0.192	5.221	IUE/STIS	3.272 ± 0.016	3.303 ± 0.011
0.200	5.011	IUE/STIS	3.162 ± 0.015	3.365 ± 0.018
0.208	4.809	IUE/STIS	3.026 ± 0.014	3.384 ± 0.012
0.217	4.615	IUE/STIS	2.894 ± 0.014	3.420 ± 0.040
0.226	4.430	IUE/STIS	2.735 ± 0.012	3.170 ± 0.028
0.235	4.251	IUE/STIS	2.571 ± 0.015	2.831 ± 0.023
0.245	4.080	IUE/STIS	2.409 ± 0.010	2.659 ± 0.015
0.255	3.916	IUE/STIS	2.328 ± 0.011	2.536 ± 0.007
0.266	3.759	IUE/STIS	2.174 ± 0.009	2.318 ± 0.011
0.277	3.607	IUE/STIS	2.091 ± 0.010	2.353 ± 0.032
0.289	3.462	IUE/STIS	1.968 ± 0.009	2.203 ± 0.023
0.301	3.323	IUE/STIS	1.888 ± 0.010	2.188 ± 0.007
0.363	2.756	JohnU	1.514 ± 0.037	1.684 ± 0.000
0.438	2.284	JohnB	1.349 ± 0.012	1.400 ± 0.007
0.544	1.837	JohnV ^a	1.021 ± 0.012	1.017 ± 0.000
1.231	0.812	JohnJ	0.324 ± 0.069	0.293 ± 0.049
1.622	0.617	JohnH	0.125 ± 0.081	0.162 ± 0.049
2.174	0.460	JohnK	0.062 ± 0.104	0.055 ± 0.081

^aThe average $A(\lambda)/A(V)$ values at V band are not exactly 1.0 due to the use of the SED fitting based $E(55 - 44)$ values corrected for $E(B - V)_{\text{MW}}$ for the $E(\lambda - V)/E(B - V)$ normalized curves. As discussed in §3.1, $E(55 - 44)$ is close to but not exactly $E(B - V)$.

the IRAC 8 μm photometry that measures the strong 7.6 and 8.5 μm features that Massa et al. (2022) found were correlated with the 2175 Å bump in the MW. All measurements are by definition normalized to the total amount of dust, with q_{PAH} normalized to the total mass of dust grains and extinc-

tion values are normalized to the total dust column as measured by $E(B - V)$.

Looking at just the SMC points in Fig. 8, there is no clear correlation. For example, there is a large range of q_{PAH} values for 2175 Å bump areas around zero and a large range of 2175 Å areas for q_{PAH} values around 1%. Combining the SMC measurements with those from the LMC (Misselt et al. 1999; Chasten et al. 2019), a different picture emerges where the two measurements are clearly correlated. To illustrate this point, a linear fit with outlier removal that accounts for the significant uncertainties on both the x and y values (Gordon et al. 2023) was done. The data points are scattered around the linear fit lines with a larger scatter than their uncertainties would predict. The deviations from the linear fit could very well be explained by variations between the pencil beam extinction measurements and the 42'' spatially averaged q_{PAH} measurements. Higher spatial resolution q_{PAH} observations like those possible with JWST would test this explanation of the scatter.

5. SMC, LMC, AND MW COMPARISONS

In this section, we analyze the details of the SMC extinction curves in context with equivalent measurements in the MW and LMC. The SMC extinction curves have significant variation and how this variation compares to what is seen in these other two galaxies is expected to provide insight into dust grain evolution as has already been discussed by Gordon et al. (2003). The previous subsection (§4.3) illustrates the strength of combining SMC and measurements from another galaxy. It was after adding the LMC measurements that the correlation between the 2175 Å bump and q_{PAH} became clear.

5.1. General Sightline Properties

While the overall impression gained from SMC extinction is that it is markedly and systematically different from that seen in the MW and LMC, nevertheless there is some overlap and some continuity in their properties. To illustrate this, we begin by plotting in Fig. 9 the general properties of the 22 sightlines with $E(B - V)_{\text{SMC}} > 0.1$ along with existing samples for the MW and LMC. Note that starting here all the extinction measurements discussed are for the SMC only quantities (e.g., $E(B - V)_{\text{SMC}} = E(B - V)$).

The $R(V)$ values for most of the SMC sightlines fall within the range of those seen in the MW and LMC. For the gas-to-dust values as measured by $N(HI)/A(V)$, the right panel of Fig. 9 shows that these values are generally higher than those found in the MW or LMC. This is expected as the gas-to-dust ratio is a function of metallicity and the SMC is more metal poor than both the MW and LMC. The average $N(HI)/A(V)$ value for the SMC of $(18.7 \pm 2.6) \times 10^{21} \text{ H cm}^{-2} \text{ mag}^{-1}$ is higher than the previously the measured value of $(13.2 \pm 1.0) \times 10^{21} \text{ H cm}^{-2} \text{ mag}^{-1}$ (Gordon et al. 2003) likely due to this value being based on only four sightlines. Our average is lower than the more recent value of $(27.5 \pm 3.5) \times 10^{21} \text{ H cm}^{-2} \text{ mag}^{-1}$ (Yanchulova Merica-Jones et al. 2021a) possibly due to this value being measured

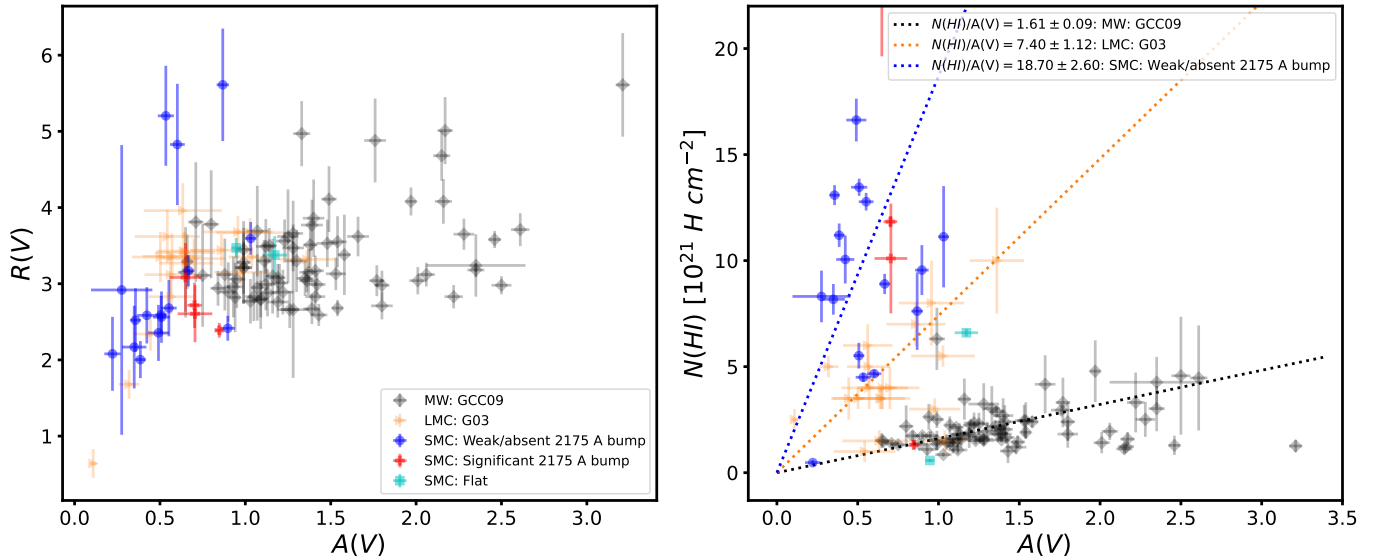


Figure 9. The general sample properties are shown. The dust grain size average measure $R(V)$ is plotted versus the dust column $A(V)$ on the left. On the right, the gas column as measured by $N(HI)$ is plotted versus the dust column $A(V)$ measured in magnitudes. Note that the measurement for MR12 10 is off the top of the plot and only the bottom error bar of this very uncertain measurement shown. In addition to the SMC subsamples from this paper, the existing LMC sample (Misselt et al. 1999; Gordon et al. 2003), and MW (Gordon et al. 2009) are shown. The dotted lines give the average $N(HI)/A(V)$ for the three samples with enough measurements to be meaningful. The average $N(HI)/A(V)$ values and uncertainties are given in the legend. The Gordon et al. (2009) sample is shown as it is the only large MW sample with full UV extinction curves and measured $N(HI)$ values (Gordon et al. 2009; Van De Putte et al. 2023).

in a small region of the SMC. In addition there is a larger scatter than explained by measurement uncertainties in the individual values.

The values of $N(HI)/A(V)$ do not scale linearly with the ratio to the MW metallicity. The ratio of average $N(HI)/A(V)$ to average $N(HI)/A(V)_{MW}$ are 12 and 5 for the SMC and LMC, yet the same ratio with metallicities are only 5 and 2 (Russell & Dopita 1992; Domínguez-Guzmán et al. 2022). It is striking that there is substantial overlap in the individual sightline $N(HI)/A(V)$ values between each galaxy. This is not a function of the dust column, as all three galaxies have measured $A(V)$ values that range between 0.5 and 1.0 and all show a range of $N(HI)$ values for this $A(V)$ range. In fact, there are sightlines in the SMC (and LMC) that have MW gas-to-dust ratios. This clearly indicates that $N(HI)/A(V)$ is dependent on more than just the galaxy metallicity.

5.2. UV Parameter Correlations

The parameterized behavior of the SMC UV extinction curves versus dust column $A(V)$ are plotted in Fig. 10 along with measurement for the LMC and MW. These plots clearly show that the SMC (and LMC) sightlines generally probe lower dust columns than have been measured in the MW. This is explained as MW studies generally use a cutoff of $E(B - V) \sim 0.2$ (Valencic et al. 2004; Fitzpatrick & Massa 2007; Gordon et al. 2009). Lower $E(B - V)$ values can be probed in the MW to lower dust columns (Fitzpatrick & Massa 2005), it is just not usually done. The plots illustrate

that the SMC sightlines generally have lower UV intercepts (C_1), 2175 Å bump strengths (B_3), and far-UV rises (C_4) than the MW. The SMC sightlines have higher UV slopes (C_2) than the MW. But these statements are based on the average behavior, there are clearly sightlines in the SMC (and LMC) that are indistinguishable in the plots from the MW behavior. The four SMC sightlines with significant bumps show 2175 Å centers and widths that are shifted from the MW averages, but they are within the scatter seen in the MW that increases as $A(V)$ decreases. Salim & Narayanan (2020) suggested that the low 2175 Å strengths in the SMC were due to the low dust columns probed. With the larger SMC sample, it is clear that the lack of the 2175 Å bump is not correlated with dust column given that low B_3 values are found even beyond $A(V) = 1$ where high B_3 values are seen in the MW.

The correlations between UV extinction parameters C_1 , C_2 , B_3 , and C_4 are shown in Fig. 11. The bump center x_o and width γ are not shown as no significant correlations are seen. The two “flat” SMC sightlines have been omitted to avoid biasing the fitting with curves that may be strongly impacted by systematic uncertainties. The known strong correlation between C_1 and C_2 is seen to extend over a large range of values and the linear fit coefficients agree with and extend previous work (Fitzpatrick & Massa 2007). This correlation indicates that the UV extinction curve variations pivot around a point at a specific wavelength likely due to normalizing the extinction curves by $E(B - V)$. There are correlations seen between C_2 , B_3 , and C_4 and these are much clearer than

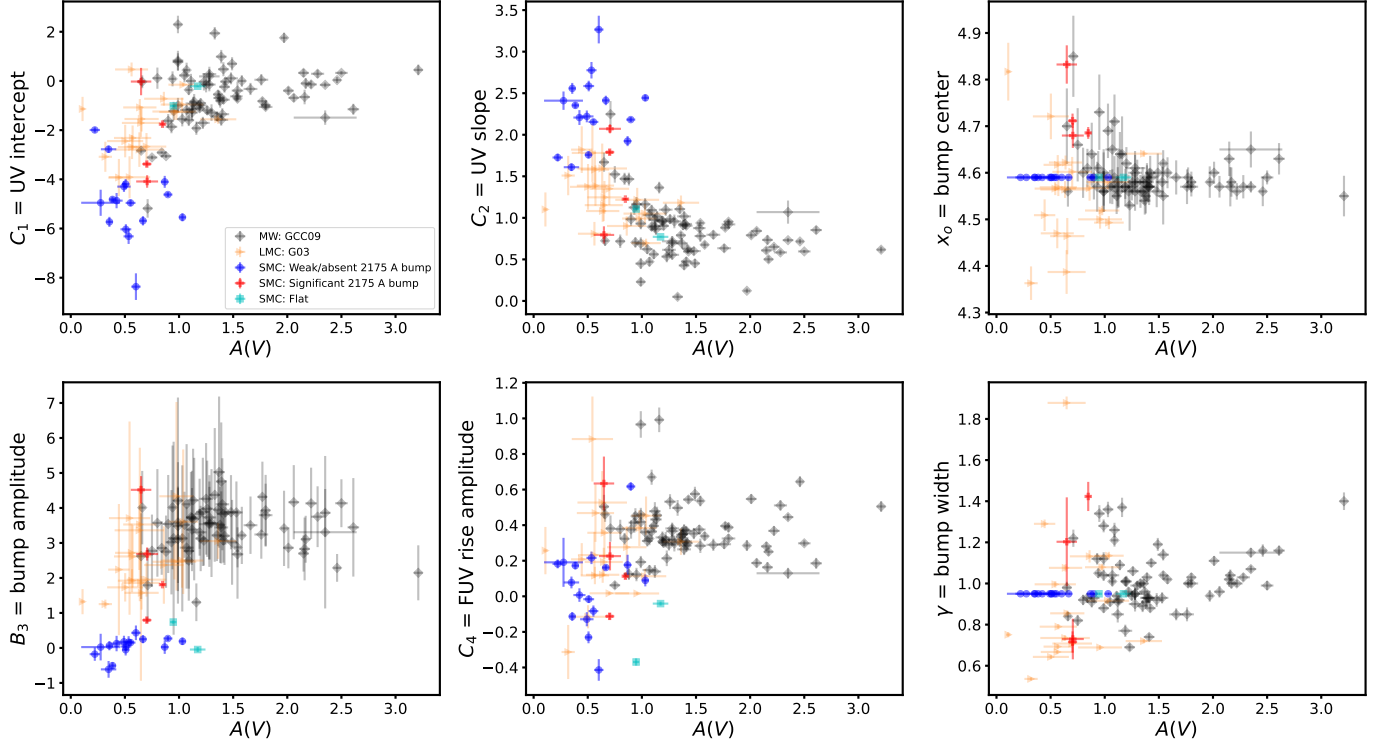


Figure 10. The FM90 parameters are plotted versus dust column density as measured by $A(V)$ in magnitudes. The behavior of MW sightlines is illustrated by the (Gordon et al. 2009) sample. The LMC sightlines are from Gordon et al. (2003). The sightlines with weak/absent 2175 Å bumps used fixed values for x_0 and γ .

previously seen (Gordon et al. 2003) due to the larger SMC sample and expanded MW sample. Linear fits were done that account for the uncertainties on both quantities (Gordon et al. 2023), but not the covariance between them as covariance is not available for the LMC and SMC samples. Regardless, the variations seen are much larger than the uncertainties and so the correlations between parameters cannot be explained by uncertainty covariance.

The correlations indicate that as the 2175 Å bump strength weakens, far-UV rise also weakens, and the UV slope strengthens. This is evidence that there is a family of curves with correlated changes across the UV. This is reminiscent of the family of curves that correlates with $R(V)$ to describe the average behavior of MW extinction (Cardelli et al. 1989; Gordon et al. 2023). Yet the family of curves indicated shows much stronger variation and is not correlated with $R(V)$ given the $R(V)$ values are similar for all the samples (see Fig. 10).

5.3. Gas-to-Dust Correlations

Gordon et al. (2003) speculated that the large variations in the FM90 parameters seen may be correlated with gas-to-dust as measured by $N(HI)/A(V)$. Fig. 12 plots $N(HI)/A(V)$ versus C_2 , B_3 , and C_4 as well as $A(V)$. The $N(HI)/A(V)$ versus $A(V)$ plot shows that while the average gas-to-dust value decreases from the SMC to the LMC to the MW, there are sightlines in each galaxy that have

$N(HI)/A(V)$ ratios that are like one or both of the other galaxies. In particular, the SMC shows that some sightlines have $N(HI)/A(V)$ values like those seen in the LMC and MW. From the other panels it is seen that the UV slope C_2 and 2175 Å bump amplitude B_3 are clearly correlated with $N(HI)/A(V)$. The correlation with the FUV rise amplitude C_4 is present, but significantly weaker.

The correlations of the UV parameters with $N(HI)/A(V)$ indicates that the extinction curve shape variations may be traced by variations in the gas-to-dust ratio. The gas-to-dust ratio varies with metallicity as dust is composed almost entirely of metals (i.e., carbonaceous and silicate grains) and the impact of accretion/ablation of gas phase atoms onto and off of dust grains. The metallicity is not seen to vary significantly across the LMC or SMC (Russell & Dopita 1992; Domínguez-Guzmán et al. 2022) and neither would the $N(HI)/A(V)$ ratio predicted by metallicity alone. Thus variations in the $N(HI)/A(V)$ ratio are most likely due to accretion and/or ablation of dust grains. The SMC (and LMC) show variations of up to a factor of 10 in the $N(HI)/A(V)$ ratios, while the MW shows a much smaller variation. The smaller MW variation may be due to the fact we observe from inside the MW and hence the dust extinction probes a relatively small region 1–2 kpc around the Sun (Valencic et al. 2004). While for the LMC and SMC, we probe sightlines across the face of both galaxies. However, the SMC in particular has considerable line-of-sight depth

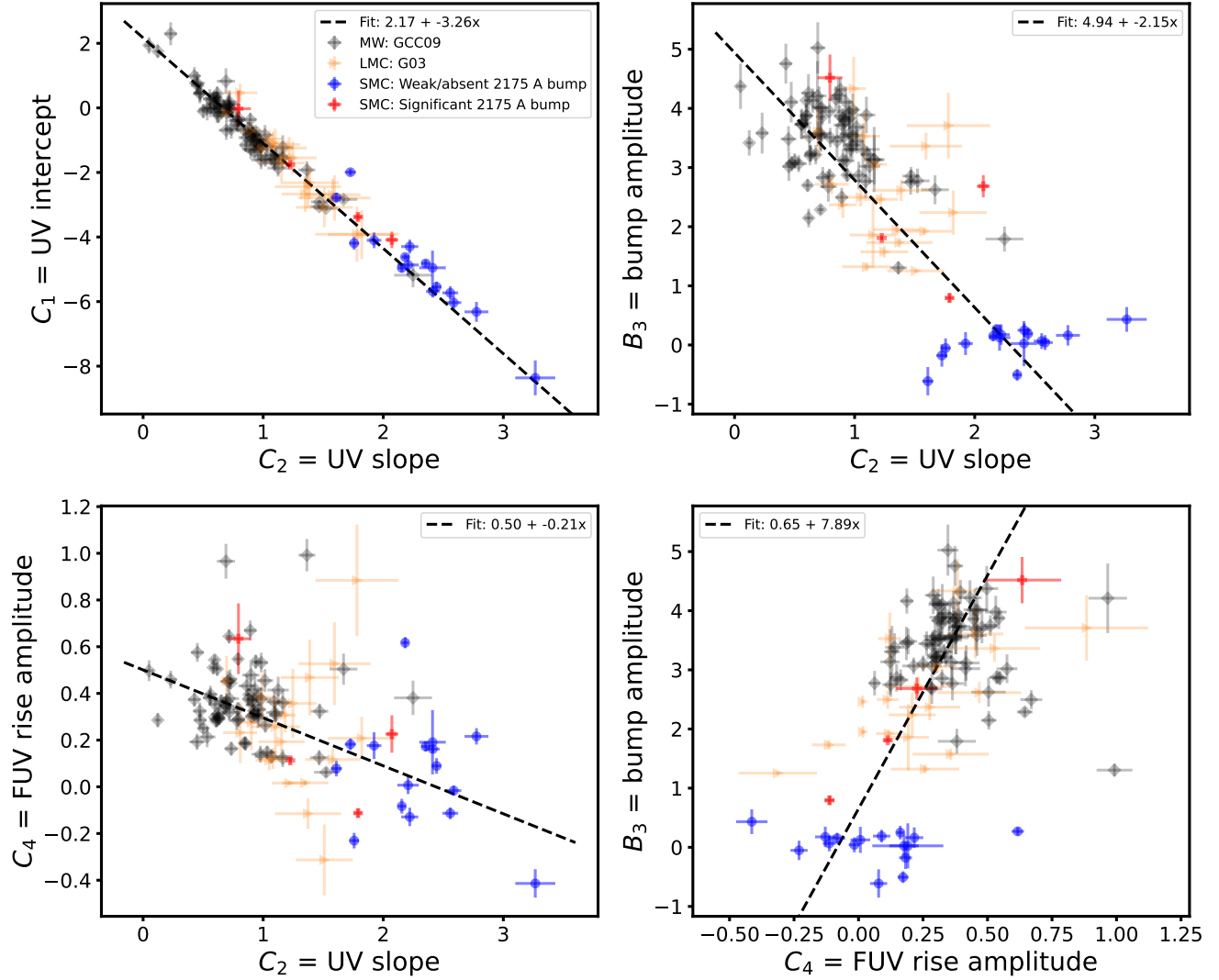


Figure 11. The behavior of the FM90 parameters versus each other is shown. The behavior of MW sightlines is illustrated by the (Gordon et al. 2009) sample and the LMC sightlines from Gordon et al. (2003). Linear fits accounting for the uncertainties on both axes are shown (Gordon et al. 2023). Note that the MW and LMC B_3 uncertainties have been approximately reduced to account for the strong correlations between C_3 and γ as they were not fit with B_3 explicitly and their covariances were not reported in the literature. Only one of the three possible similar MW samples are used to avoid the fitting over-weighting the MW points in comparison to the LMC and SMC.

(~ 20 kpc), and may be composed of distinct structures (Murray et al. 2024), and therefore the position of each UV-bright star along the line of sight will affect the interpretation of its $N(HI)/A(V)$ ratio.

A full investigation of the variations of extinction with $N(HI)/A(V)$ is beyond the scope of this paper. Such an investigation must also include a simultaneous accounting for the known MW extinction variations that are strongly correlated with $R(V)$ (Cardelli et al. 1989; Gordon et al. 2023). The potential exists for a two parameter relationship based on $R(V)$ and $N(HI)/A(V)$ extending the existing MW $R(V)$ dependent extinction relationship that would explain the variations seen in the MW, LMC, and SMC. Investigating if an $R(V)$ and $N(HI)/A(V)$ extinction relationship is possible

will be presented in a followup paper, including a complete accounting for the full covariance and outliers. That such a two parameter relationship is possible, is clear given that it has already been proposed based on the 2175 Å bump amplitude (Zagury 2007) or an arbitrary f_A mixture coefficient (Gordon et al. 2016). Our finding that the variations are correlated with the gas-to-dust ratio provides a physical basis that is not a specific property of the extinction curve itself (i.e., 2175 Å bump amplitude) or an arbitrary parameter (i.e., f_A).

6. SUMMARY

We have presented a sample of UV extinction curves for the SMC based on UV spectra from the IUE archive and

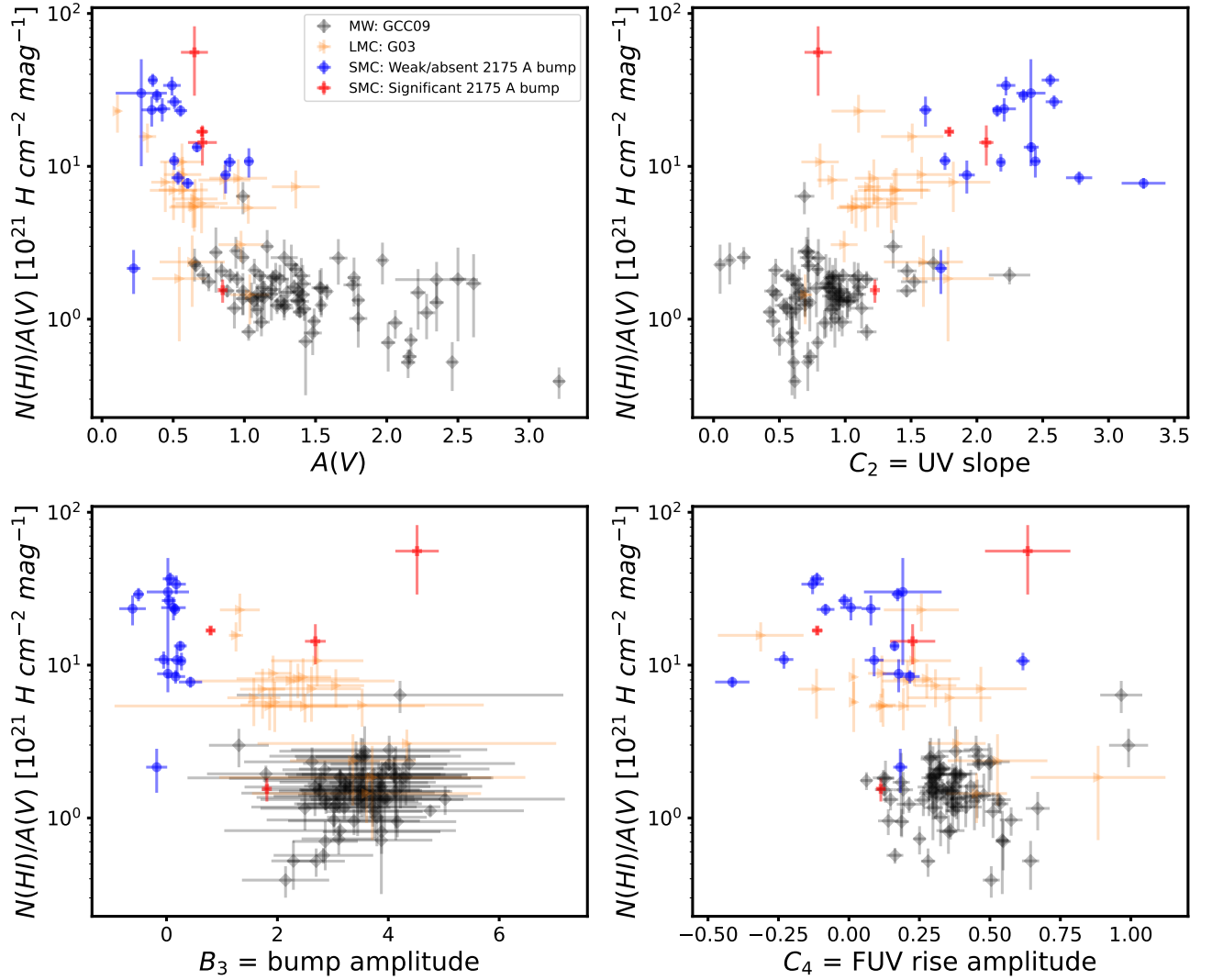


Figure 12. The gas-to-dust ratio $N(HI)/A(V)$ is shown versus selected extinction properties. The plot of $N(HI)/A(V)$ versus $A(V)$ (in magnitudes) shows the general behavior of gas-to-dust increasing from the MW to the LMC to the SMC. The plots of $N(HI)/A(V)$ versus C_2 , B_3 , and C_4 show clear correlations. The plot of $N(HI)/A(V)$ versus the UV intercept C_1 is not shown as it is very similar to that for C_2 given the extremely strong correlation between these two parameters.

three HST/STIS programs. This sample expands the number of sightlines with $E(B - V)_{SMC} > 0.1$ and UV spectroscopic measurements including $N(HI)$ from $Ly\alpha$ from five to 22. All the extinction curves have been determined by comparison to stellar atmosphere models and corrected for MW foreground extinction. Of these sightlines, 16 are seen that are strongly rising to shorter wavelengths with no significant 2175 Å bump, four have significant 2175 Å bumps, and two are relatively flat in the UV with no significant 2175 Å bumps.

The sightlines with and without 2175 Å bumps are both distributed throughout the SMC. There are two regions that show strong variation in extinction curve shape over small spatial scales. This confirms and expands the results seen in

the combination of the two previous studies (Gordon et al. 2003; Maíz Apellániz & Rubio 2012).

We present the SMC Average and SMC Bumps averages based on the weak/absent and significant 2175 Å bump samples, respectively. The SMC Average curve is based on 16 sightlines and is extremely similar to that presented for the SMC Bar based on four sightlines by (Gordon et al. 2003). Interestingly, the SMC Average $R(V) = 3.13$ very similar to the MW average $R(V)$ yet the UV extinction curve is very different. The SMC Bumps curve shows a weaker 2175 Å than the MW equivalent curve for the SMC Bumps $R(V) = 2.59$. These averages illustrate that the majority of the SMC curves are not explained by the MW $R(V)$ dependent relationship as shown in this paper and previously by Gordon et al. (2003).

The hypothesis that the 2175 Å bump and mid-IR carbonaceous (aka PAH) features is tested by correlating the 2175 Å bump area with the mass fraction of “PAH grains” q_{PAH} . We find that these two measurements are correlated in the combined SMC and LMC samples supporting this hypothesis. This extends the results from the MW (Massa et al. 2022) to lower metallicities and q_{PAH} values. In addition, we find a suggestive correlation of q_{PAH} with the FUV rise amplitude indicating this feature may also be due to the same grains.

The UV extinction as parameterized by the UV intercept C_1 , UV slope C_2 , amplitude of the 2175 Å bump B_3 , and far-UV rise amplitude C_4 are seen in general to have values that are quite different from those seen in the LMC and MW. Yet, there are SMC sightlines that have such parameters that easily fall with those seen in the LMC and MW. These parameters are seen to be strongly correlated with each other in the combined SMC, LMC, and MW results indicating that as the UV slope becomes steeper, the 2175 Å bump and the far-UV rise becomes weaker. This indicates that there is a family of curves that likely explains the majority of the variations seen. We find that the UV parameters are roughly correlated with gas-to-dust as measured by $N(HI)/A(V)$ confirming the tentative suggestion of Gordon et al. (2003). Thus, it is possible that the general behavior of dust extinction in the SMC, LMC, and MW may be explained by two parameters. These two parameters could be $N(HI)/A(V)$ as shown here and $R(V)$ as has been shown in the MW (Cardelli et al. 1989;

Gordon et al. 2023). Further investigations of a two parameter relationship will be presented in a followup paper.

The code used for the analysis and plots is available^{2 3 4} (Gordon 2024a; Gordon & Decleir 2024; Gordon 2024b). The STIS data used in this paper can be found in MAST: 10.17909/qw8x-9y41. The extinction curves measured and analyzed are available (Gordon 2024c). The averages are available as the G24_SMCavg and G24_SMCBumps average models in the dust_extinction package⁵ (Gordon 2024d).

We thank Petia Yanchulova Merica-Jones for providing the SMIDGE photometry for the MR12 stars. This paper benefited from discussions of preliminary results with the ISM*@ST group⁶. This research is based on observations made with the NASA/ESA Hubble Space Telescope obtained from the Space Telescope Science Institute, which is operated by the Association of Universities for Research in Astronomy, Inc., under NASA contract NAS 5–26555. These observations are associated with programs 8198, 12258, and 14225.

Facilities: IUE, HST (STIS)

Software: Astropy (Astropy Collaboration et al. 2013; Price-Whelan et al. 2018; Astropy Collaboration et al. 2022); dust_extinction (Gordon 2024d); measure_extinction (Gordon & Decleir 2024)

REFERENCES

- Ardeberg, A., & Maurice, E. 1977, A&AS, 30, 261
- Astropy Collaboration, Robitaille, T. P., Tollerud, E. J., et al. 2013, A&A, 558, A33, doi: 10.1051/0004-6361/201322068
- Astropy Collaboration, Price-Whelan, A. M., Lim, P. L., et al. 2022, ApJ, 935, 167, doi: 10.3847/1538-4357/ac7c74
- Azzopardi, M., Vigneau, J., & Macquet, M. 1975, A&AS, 22, 285
- Basinski, J. M., Bok, B. J., & Bok, P. F. 1967, MNRAS, 137, 55, doi: 10.1093/mnras/137.1.55
- Bell, C. P. M., Cioni, M.-R. L., Wright, A. H., et al. 2019, MNRAS, 489, 3200, doi: 10.1093/mnras/stz2325
- Bohlin, R., & Hartig, G. 1998, Clear Aperture Fractional Transmission for Point Sources, Instrument Science Report, STIS 1998–20, (Baltimore: STScI), Tech. rep.
- Bohlin, R. C. 1975, ApJ, 200, 402, doi: 10.1086/153803
- Bohlin, R. C., Mészáros, S., Fleming, S. W., et al. 2017, AJ, 153, 234, doi: 10.3847/1538-3881/aa6ba9
- Bohlin, R. C., Savage, B. D., & Drake, J. F. 1978, ApJ, 224, 132, doi: 10.1086/156357
- Buat, V., Noll, S., Burgarella, D., et al. 2012, A&A, 545, A141, doi: 10.1051/0004-6361/201219405
- Calzetti, D., Bohlin, R. C., Gordon, K. D., Witt, A. N., & Bianchi, L. 1995, ApJL, 446, L97, doi: 10.1086/187939
- Calzetti, D., Kinney, A. L., & Storchi-Bergmann, T. 1994, ApJ, 429, 582, doi: 10.1086/174346
- Cardelli, J. A., Clayton, G. C., & Mathis, J. S. 1989, ApJ, 345, 245, doi: 10.1086/167900
- Chastenet, J., Sandstrom, K., Chiang, I.-D., et al. 2019, ApJ, 876, 62, doi: 10.3847/1538-4357/ab16cf
- Clayton, G. C., Gordon, K. D., Bianchi, L. C., et al. 2015, ApJ, 815, 14, doi: 10.1088/0004-637X/815/1/14
- Cutri, R., Skrutskie, M., Van Dyk, S., et al. 2008, Explanatory Supplement to the 2MASS All Sky Data Release, Tech. rep., IPAC
- Decleir, M., Gordon, K. D., Andrews, J. E., et al. 2022, ApJ, 930, 15, doi: 10.3847/1538-4357/ac5d8e
- Diplas, A., & Savage, B. D. 1994, ApJ, 427, 274, doi: 10.1086/174139
- Domínguez-Guzmán, G., Rodríguez, M., García-Rojas, J., Esteban, C., & Toribio San Cipriano, L. 2022, MNRAS, 517, 4497, doi: 10.1093/mnras/stac2974
- Draine, B. T., & Li, A. 2007, ApJ, 657, 810, doi: 10.1086/511055

² https://github.com/karllark/hst_smc_ext

³ https://github.com/karllark/measure_extinction

⁴ https://github.com/karllark/extinction_ensemble_props

⁵ https://github.com/karllark/dust_extinction

- Duley, W. W., & Williams, D. A. 1981, *MNRAS*, 196, 269, doi: [10.1093/mnras/196.2.269](https://doi.org/10.1093/mnras/196.2.269)
- Elíasdóttir, Á., Fynbo, J. P. U., Hjorth, J., et al. 2009, *ApJ*, 697, 1725, doi: [10.1088/0004-637X/697/2/1725](https://doi.org/10.1088/0004-637X/697/2/1725)
- Evans, C. J., Howarth, I. D., Irwin, M. J., Burnley, A. W., & Harries, T. J. 2004, *MNRAS*, 353, 601, doi: [10.1111/j.1365-2966.2004.08096.x](https://doi.org/10.1111/j.1365-2966.2004.08096.x)
- Evans, C. J., Lennon, D. J., Smartt, S. J., & Trundle, C. 2006, *A&A*, 456, 623, doi: [10.1051/0004-6361:20064988](https://doi.org/10.1051/0004-6361:20064988)
- Fitzpatrick, E. L. 1985, *ApJ*, 299, 219, doi: [10.1086/163694](https://doi.org/10.1086/163694)
- Fitzpatrick, E. L., & Massa, D. 1986, *ApJ*, 307, 286, doi: [10.1086/164415](https://doi.org/10.1086/164415)
- . 1990, *ApJS*, 72, 163, doi: [10.1086/191413](https://doi.org/10.1086/191413)
- . 2005, *AJ*, 130, 1127, doi: [10.1086/431900](https://doi.org/10.1086/431900)
- . 2007, *ApJ*, 663, 320, doi: [10.1086/518158](https://doi.org/10.1086/518158)
- Fitzpatrick, E. L., Massa, D., Gordon, K. D., Bohlin, R., & Clayton, G. C. 2019, *ApJ*, 886, 108, doi: [10.3847/1538-4357/ab4c3a](https://doi.org/10.3847/1538-4357/ab4c3a)
- Foreman-Mackey, D., Hogg, D. W., Lang, D., & Goodman, J. 2013, *PASP*, 125, 306, doi: [10.1086/670067](https://doi.org/10.1086/670067)
- Gaia Collaboration. 2018, *VizieR Online Data Catalog*, I/345
- Gordon, K. 2024a, *hst_smc_ext*, 1.0, Zenodo, doi: [10.5281/zenodo.11187091](https://doi.org/10.5281/zenodo.11187091)
- . 2024b, *extinction_ensemble_props*, 1.01, Zenodo, doi: [10.5281/zenodo.11187409](https://doi.org/10.5281/zenodo.11187409)
- . 2024c, *Data for SMC UV Expanded Sample paper*, 1.0, Zenodo, doi: [10.5281/zenodo.11187458](https://doi.org/10.5281/zenodo.11187458)
- . 2024d, *dust_extinction*, v1.4.1, Zenodo, doi: [10.5281/zenodo.11235336](https://doi.org/10.5281/zenodo.11235336)
- Gordon, K., & Declair, M. 2024, *measure_extinction*, 1.3, Zenodo, doi: [10.5281/zenodo.11186967](https://doi.org/10.5281/zenodo.11186967)
- Gordon, K. D., Calzetti, D., & Witt, A. N. 1997, *ApJ*, 487, 625, doi: [10.1086/304654](https://doi.org/10.1086/304654)
- Gordon, K. D., Cartledge, S., & Clayton, G. C. 2009, *ApJ*, 705, 1320, doi: [10.1088/0004-637X/705/2/1320](https://doi.org/10.1088/0004-637X/705/2/1320)
- Gordon, K. D., & Clayton, G. C. 1998, *ApJ*, 500, 816, doi: [10.1086/305774](https://doi.org/10.1086/305774)
- Gordon, K. D., Clayton, G. C., Declair, M., et al. 2023, *ApJ*, 950, 86, doi: [10.3847/1538-4357/accb59](https://doi.org/10.3847/1538-4357/accb59)
- Gordon, K. D., Clayton, G. C., Misselt, K. A., Landolt, A. U., & Wolff, M. J. 2003, *ApJ*, 594, 279, doi: [10.1086/376774](https://doi.org/10.1086/376774)
- Gordon, K. D., Meixner, M., Meade, M. R., et al. 2011, *AJ*, 142, 102, doi: [10.1088/0004-6256/142/4/102](https://doi.org/10.1088/0004-6256/142/4/102)
- Gordon, K. D., Roman-Duval, J., Bot, C., et al. 2014, *ApJ*, 797, 85, doi: [10.1088/0004-637X/797/2/85](https://doi.org/10.1088/0004-637X/797/2/85)
- Gordon, K. D., Fouesneau, M., Arab, H., et al. 2016, *ApJ*, 826, 104, doi: [10.3847/0004-637X/826/2/104](https://doi.org/10.3847/0004-637X/826/2/104)
- Joblin, C., Leger, A., & Martin, P. 1992, *ApJL*, 393, L79, doi: [10.1086/186456](https://doi.org/10.1086/186456)
- Kalberla, P. M. W., & Haud, U. 2015, *A&A*, 578, A78, doi: [10.1051/0004-6361/201525859](https://doi.org/10.1051/0004-6361/201525859)
- Kalberla, P. M. W., McClure-Griffiths, N. M., Pisano, D. J., et al. 2010, *A&A*, 521, A17, doi: [10.1051/0004-6361/200913979](https://doi.org/10.1051/0004-6361/200913979)
- Kato, D., Nagashima, C., Nagayama, T., et al. 2007, *PASJ*, 59, 615, doi: [10.1093/pasj/59.3.615](https://doi.org/10.1093/pasj/59.3.615)
- Kriek, M., & Conroy, C. 2013, *ApJL*, 775, L16, doi: [10.1088/2041-8205/775/1/L16](https://doi.org/10.1088/2041-8205/775/1/L16)
- Lanz, T., & Hubeny, I. 2003, *ApJS*, 146, 417, doi: [10.1086/374373](https://doi.org/10.1086/374373)
- . 2007, *ApJS*, 169, 83, doi: [10.1086/511270](https://doi.org/10.1086/511270)
- Lennon, D. J. 1997, *A&A*, 317, 871
- Lequeux, J., Maurice, E., Prevot-Burnichon, M.-L., Prevot, L., & Rocca-Volmerange, B. 1982, *A&A*, 113, L15
- Li, A., & Draine, B. T. 2001, *ApJ*, 554, 778, doi: [10.1086/323147](https://doi.org/10.1086/323147)
- Liszt, H. 2014, *ApJ*, 783, 17, doi: [10.1088/0004-637X/783/1/17](https://doi.org/10.1088/0004-637X/783/1/17)
- Maíz Apellániz, J., & Rubio, M. 2012, *A&A*, 541, A54, doi: [10.1051/0004-6361/201118712](https://doi.org/10.1051/0004-6361/201118712)
- Markov, V., Gallerani, S., Pallottini, A., et al. 2023, *A&A*, 679, A12, doi: [10.1051/0004-6361/202346723](https://doi.org/10.1051/0004-6361/202346723)
- Martayan, C., Frémat, Y., Hubert, A.-M., et al. 2007, *A&A*, 462, 683, doi: [10.1051/0004-6361:20065076](https://doi.org/10.1051/0004-6361:20065076)
- Massa, D., Gordon, K. D., & Fitzpatrick, E. L. 2022, *ApJ*, 925, 19, doi: [10.3847/1538-4357/ac3825](https://doi.org/10.3847/1538-4357/ac3825)
- Massa, D., Savage, B. D., & Fitzpatrick, E. L. 1983, *ApJ*, 266, 662, doi: [10.1086/160813](https://doi.org/10.1086/160813)
- Mathis, J. S. 1994, *ApJ*, 422, 176, doi: [10.1086/173715](https://doi.org/10.1086/173715)
- Mathis, J. S., & Cardelli, J. A. 1992, *ApJ*, 398, 610, doi: [10.1086/171886](https://doi.org/10.1086/171886)
- McClure-Griffiths, N. M., Pisano, D. J., Calabretta, M. R., et al. 2009, *ApJS*, 181, 398, doi: [10.1088/0067-0049/181/2/398](https://doi.org/10.1088/0067-0049/181/2/398)
- Mermilliod, J. C. 1997, *VizieR Online Data Catalog*, II/168
- Misselt, K. A., Clayton, G. C., & Gordon, K. D. 1999, *ApJ*, 515, 128, doi: [10.1086/307010](https://doi.org/10.1086/307010)
- Murray, C. E., Hasselquist, S., Peek, J. E. G., et al. 2024, *ApJ*, 962, 120, doi: [10.3847/1538-4357/ad1591](https://doi.org/10.3847/1538-4357/ad1591)
- Nandy, K., McLachlan, A., Thompson, G. I., et al. 1982, *MNRAS*, 201, 1P, doi: [10.1093/mnras/201.1.1P](https://doi.org/10.1093/mnras/201.1.1P)
- Nidever, D. L., Olsen, K., Walker, A. R., et al. 2017, *AJ*, 154, 199, doi: [10.3847/1538-3881/aa8d1c](https://doi.org/10.3847/1538-3881/aa8d1c)
- Noll, S., Pierini, D., Pannella, M., & Savaglio, S. 2007, *A&A*, 472, 455, doi: [10.1051/0004-6361:20077067](https://doi.org/10.1051/0004-6361:20077067)
- Noll, S., Pierini, D., Cimatti, A., et al. 2009, *A&A*, 499, 69, doi: [10.1051/0004-6361/200811526](https://doi.org/10.1051/0004-6361/200811526)
- Prevot, M. L., Lequeux, J., Prevot, L., Maurice, E., & Rocca-Volmerange, B. 1984, *A&A*, 132, 389
- Price-Whelan, A. M., Sipőcz, B. M., Günther, H. M., et al. 2018, *AJ*, 156, 123, doi: [10.3847/1538-3881/aabc4f](https://doi.org/10.3847/1538-3881/aabc4f)
- Rieke, G. H., Rieke, M. J., & Paul, A. E. 1989, *ApJ*, 336, 752, doi: [10.1086/167047](https://doi.org/10.1086/167047)

- Russell, S. C., & Dopita, M. A. 1992, *ApJ*, 384, 508, doi: [10.1086/170893](https://doi.org/10.1086/170893)
- Salim, S., & Narayanan, D. 2020, *ARA&A*, 58, 529, doi: [10.1146/annurev-astro-032620-021933](https://doi.org/10.1146/annurev-astro-032620-021933)
- Sanduleak, N. 1969, *AJ*, 74, 877, doi: [10.1086/110875](https://doi.org/10.1086/110875)
- Schady, P., Dwelly, T., Page, M. J., et al. 2012, *A&A*, 537, A15, doi: [10.1051/0004-6361/201117414](https://doi.org/10.1051/0004-6361/201117414)
- Schlegel, D. J., Finkbeiner, D. P., & Davis, M. 1998, *ApJ*, 500, 525, doi: [10.1086/305772](https://doi.org/10.1086/305772)
- Schwering, P. B. W., & Israel, F. P. 1991, *A&A*, 246, 231
- Smith Neubig, M. M., & Bruhweiler, F. C. 1997, *AJ*, 114, 1951, doi: [10.1086/118617](https://doi.org/10.1086/118617)
- Valencic, L. A., Clayton, G. C., & Gordon, K. D. 2004, *ApJ*, 616, 912, doi: [10.1086/424922](https://doi.org/10.1086/424922)
- Valencic, L. A., Clayton, G. C., Gordon, K. D., & Smith, T. L. 2003, *ApJ*, 598, 369, doi: [10.1086/378802](https://doi.org/10.1086/378802)
- Van De Putte, D., Cartledge, S. I. B., Gordon, K. D., Clayton, G. C., & Roman-Duval, J. 2023, *ApJ*, 944, 33, doi: [10.3847/1538-4357/ac9902](https://doi.org/10.3847/1538-4357/ac9902)
- Vijh, U. P., Witt, A. N., & Gordon, K. D. 2003, *ApJ*, 587, 533, doi: [10.1086/368344](https://doi.org/10.1086/368344)
- Walborn, N. R. 1983, *ApJ*, 265, 716, doi: [10.1086/160716](https://doi.org/10.1086/160716)
- Whittet, D. C. B., Shenoy, S. S., Clayton, G. C., & Gordon, K. D. 2004, *ApJ*, 602, 291, doi: [10.1086/380837](https://doi.org/10.1086/380837)
- Witstok, J., Shivaee, I., Smit, R., et al. 2023, *Nature*, 621, 267, doi: [10.1038/s41586-023-06413-w](https://doi.org/10.1038/s41586-023-06413-w)
- Yanchulova Merica-Jones, P., Sandstrom, K. M., Johnson, L. C., et al. 2017, *ApJ*, 847, 102, doi: [10.3847/1538-4357/aa8a67](https://doi.org/10.3847/1538-4357/aa8a67)
- . 2021a, *ApJ*, 907, 50, doi: [10.3847/1538-4357/abc48b](https://doi.org/10.3847/1538-4357/abc48b)
- . 2021b, *ApJ*, 907, 50, doi: [10.3847/1538-4357/abc48b](https://doi.org/10.3847/1538-4357/abc48b)
- Zafar, T., Watson, D., Elíasdóttir, Á., et al. 2012, *ApJ*, 753, 82, doi: [10.1088/0004-637X/753/1/82](https://doi.org/10.1088/0004-637X/753/1/82)
- Zagury, F. 2007, *Ap&SS*, 312, 113, doi: [10.1007/s10509-007-9661-y](https://doi.org/10.1007/s10509-007-9661-y)
- Zaritsky, D., Harris, J., Thompson, I. B., & Grebel, E. K. 2004, *AJ*, 128, 1606, doi: [10.1086/423910](https://doi.org/10.1086/423910)

Table 8. Sample UBV Photometry

Name	U	B	V	$B - V$	$U - B$	Ref
2DFS 413	...	16.725 ± 0.040	16.715 ± 0.061	1
2DFS 626	15.926 ± 0.030	16.651 ± 0.030	16.483 ± 0.031	1
2DFS 662	14.120 ± 0.031	14.962 ± 0.021	14.891 ± 0.049	1
2DFS 699	13.465 ± 0.030	14.141 ± 0.023	14.063 ± 0.030	1
2DFS 3014	15.878 ± 0.035	16.633 ± 0.035	16.637 ± 0.033	1
2DFS 3030	14.143 ± 0.033	15.044 ± 0.029	15.045 ± 0.022	1
2DFS 3171	14.987 ± 0.054	15.790 ± 0.034	15.635 ± 0.024	1
AzV 4	13.835 ± 0.033	0.094 ± 0.005	-0.757 ± 0.010	2
AzV 18	12.420 ± 0.044	0.041 ± 0.006	-0.794 ± 0.021	3
AzV 23	12.244 ± 0.004	0.084 ± 0.002	-0.672 ± 0.008	3
AzV 70	12.413 ± 0.013	-0.154 ± 0.013	-1.003 ± 0.016	3
AzV 86	12.800 ± 0.035	-0.147 ± 0.015	-0.966 ± 0.005	2
AzV 132	13.630 ± 0.020	0.090 ± 0.015	-0.750 ± 0.025	2
AzV 214	13.416 ± 0.013	0.038 ± 0.007	-0.803 ± 0.007	3
AzV 218	12.643 ± 0.030	13.554 ± 0.030	13.636 ± 0.030	1
AzV 289	12.396 ± 0.026	-0.118 ± 0.009	-0.984 ± 0.013	3
AzV 380	13.534 ± 0.007	-0.109 ± 0.010	-0.918 ± 0.009	3
AzV 398	13.889 ± 0.026	0.100 ± 0.022	-0.820 ± 0.021	3
AzV 456	12.888 ± 0.019	0.109 ± 0.009	-0.785 ± 0.015	3
AzV 462	12.566 ± 0.017	-0.126 ± 0.012	-0.914 ± 0.014	1
BBB 280	14.480 ± 0.020	-0.020 ± 0.015	-0.790 ± 0.025	4
NGC330 ELS 110	...	16.330 ± 0.021	16.381 ± 0.033	1
NGC330 ELS 114	...	16.439 ± 0.023	16.491 ± 0.030	1
NGC330 ELS 116	...	16.429 ± 0.087	16.554 ± 0.062	1
SK 191	11.860 ± 0.020	-0.040 ± 0.015	-0.850 ± 0.025	5
SMC5-398	...	14.190 ± 0.032	14.221 ± 0.057	1
SMC5-3739	14.180 ± 0.020	-0.080 ± 0.015	-0.470 ± 0.025	2
SMC5-79264	...	15.297 ± 0.016	15.192 ± 0.028	1
SMC5-82923	13.688 ± 0.030	14.205 ± 0.030	14.251 ± 0.037	1

References—(1) Zaritsky et al. (2004), (2) Mermilliod (1997), (3) Gordon et al. (2003), (4) Basinski et al. (1967), (5) Ardeberg & Maurice (1977)

APPENDIX

A. PHOTOMETRY

of the MR12 stars, HST photometry from the HST SMIDGE catalog Yanchulova Merica-Jones et al. (2017, 2021b). The SMIDGE region covered a fairly small portion of the SMC, fortunately including the entire MR12 region.

The literature optical/near-infrared photometry for all the stars in our sample is given in Tables 8–10. The optical UBV photometry is given in Table 8 in the form reported in literature where roughly half reported colors and half reported magnitudes in all three bands. In Table 9 the $griz$ values are from the SMASH survey (Nidever et al. 2017) and the JHK_S values are from the IRSF survey (Kato et al. 2007). One exception is for AzV 132 where the photometry is from 2MASS (Cutri et al. 2008). Given the faintness

Table 9. Sample *griz* and *JHK_S* Photometry

Star	<i>g</i>	<i>r</i>	<i>i</i>	<i>z</i>	<i>J</i>	<i>H</i>	<i>K_S</i>
2DFS 413	16.663 ± 0.044	16.928 ± 0.039	17.106 ± 0.062	17.298 ± 0.020	16.64 ± 0.02	16.57 ± 0.04	16.68 ± 0.13
2DFS 626	16.553 ± 0.020	16.717 ± 0.022	16.851 ± 0.054	17.061 ± 0.020	16.51 ± 0.03	16.46 ± 0.03	16.57 ± 0.14
2DFS 662	14.867 ± 0.020	15.117 ± 0.020	15.288 ± 0.020	15.541 ± 0.020	15.00 ± 0.01	15.01 ± 0.02	15.04 ± 0.04
2DFS 699	13.98 ± 0.01	13.93 ± 0.01	13.91 ± 0.01
2DFS 3014	16.558 ± 0.079	16.771 ± 0.020	16.929 ± 0.020	17.145 ± 0.020	16.75 ± 0.02	16.68 ± 0.05	16.99 ± 0.21
2DFS 3030	14.913 ± 0.029	15.166 ± 0.020	15.320 ± 0.027	15.554 ± 0.035	15.12 ± 0.01	15.17 ± 0.02	15.15 ± 0.04
2DFS 3171	15.621 ± 0.023	15.747 ± 0.035	15.840 ± 0.027	16.012 ± 0.033	15.49 ± 0.02	15.52 ± 0.02	15.54 ± 0.05
AzV 4	13.59 ± 0.02	13.51 ± 0.01	13.36 ± 0.02
AzV 18	12.40 ± 0.02	12.35 ± 0.01	12.33 ± 0.01
AzV 23	12.04 ± 0.01	11.98 ± 0.01	11.91 ± 0.01
AzV 70	12.79 ± 0.01	12.81 ± 0.01	12.85 ± 0.01
AzV 86	13.05 ± 0.01	13.11 ± 0.01	13.13 ± 0.01
AzV 132	13.609 ± 0.034	13.223 ± 0.037	13.120 ± 0.044
AzV 214	13.41 ± 0.01	13.38 ± 0.01	13.36 ± 0.01
AzV 218	13.87 ± 0.01	13.92 ± 0.01	13.93 ± 0.01
AzV 289	12.68 ± 0.01	12.72 ± 0.01	12.74 ± 0.02
AzV 380	13.82 ± 0.02	13.86 ± 0.01	13.91 ± 0.02
AzV 398	13.62 ± 0.01	13.57 ± 0.01	13.52 ± 0.02
AzV 456	12.82 ± 0.01	12.83 ± 0.01	12.83 ± 0.02
AzV 462	12.90 ± 0.02	12.94 ± 0.01	12.94 ± 0.02
BBB 280	14.26 ± 0.02	14.17 ± 0.01	14.02 ± 0.01
MR12 09	18.252 ± 0.029	18.544 ± 0.044	18.668 ± 0.072	18.902 ± 0.020	18.424 ± 0.066	18.378 ± 0.068	18.307 ± 0.081
MR12 11	18.513 ± 0.027	18.668 ± 0.041	18.721 ± 0.032	18.925 ± 0.020	18.220 ± 0.067	18.400 ± 0.069	18.426 ± 0.083
NGC330 ELS 110	16.265 ± 0.020	16.738 ± 0.078	16.957 ± 0.170	17.266 ± 0.020	16.96 ± 0.02	16.98 ± 0.03	17.23 ± 0.11
NGC330 ELS 114	16.312 ± 0.035	16.748 ± 0.053	16.936 ± 0.216	17.237 ± 0.020	16.92 ± 0.02	16.98 ± 0.05	16.93 ± 0.16
NGC330 ELS 116	16.328 ± 0.021	16.787 ± 0.060	17.011 ± 0.184	17.266 ± 0.038	16.91 ± 0.02	16.92 ± 0.07	16.94 ± 0.13
SK 191	12.04 ± 0.02	12.02 ± 0.01	12.02 ± 0.02
SMC5-000398	14.053 ± 0.136	14.426 ± 0.020	...	14.784 ± 0.110	14.38 ± 0.01	14.42 ± 0.01	14.38 ± 0.02
SMC5-003739	14.13 ± 0.01	14.12 ± 0.01	14.15 ± 0.02
SMC5-079264	15.182 ± 0.020	15.410 ± 0.100	15.557 ± 0.020	15.694 ± 0.384	15.20 ± 0.02	15.17 ± 0.02	15.17 ± 0.04
SMC5-082923	14.192 ± 0.020	14.490 ± 0.020	...	14.892 ± 0.020	14.46 ± 0.01	14.45 ± 0.02	14.51 ± 0.02

Table 10. Sample HST photometry

Band	MR12 09	MR12 10	MR12 11
F225W	17.362 ± 0.005	18.803 ± 0.009	17.966 ± 0.006
F275W	17.378 ± 0.004	18.648 ± 0.009	17.713 ± 0.004
F336W	17.607 ± 0.002	18.643 ± 0.004	17.784 ± 0.003
F475W	18.410 ± 0.002	19.160 ± 0.001	18.623 ± 0.001
F550M	18.391 ± 0.002	19.005 ± 0.003	18.522 ± 0.002
F814W	18.385 ± 0.001	18.880 ± 0.001	18.376 ± 0.001
F110W	18.480 ± 0.003	18.828 ± 0.002	18.410 ± 0.002
F160W	18.443 ± 0.002	18.740 ± 0.003	18.353 ± 0.002